Nonequilibrium plasma aerotaxy of size controlled GaN nanocrystals

Necip B Uner¹ and Elijah Thimsen^{1,2}

- Department of Energy, Environmental and Chemical Engineering, Washington University in St. Louis, Brookings Dr, St. Louis, MO 63130, United States of America
- ² Institute for Materials Science and Engineering, Washington University in St. Louis, 1 Brookings Dr., St. Louis, MO 63130, United States of America

E-mail: elijah.thimsen@wustl.edu

Received 13 August 2019, revised 5 November 2019 Accepted for publication 21 November 2019 Published 18 December 2019



Abstract

High quality gallium nitride (GaN) nanocrystals (NCs) are promising materials in a wide range of applications including optoelectronics, photonics and biomedical devices. Unlike II-VI semiconductors, the synthesis of free-standing GaN NCs is not well-established, and there is a need for a synthesis platform that can provide GaN NCs with tunable size and photonic properties. In this work, we present a flexible gas-phase synthesis method that can deliver crystalline, free-standing, pure GaN NCs with controlled size and narrow size distributions. The method, termed nonequilibrium plasma aerotaxy (NPA), employs an aerosol of Ga and gaseous N₂ as the precursors. The term aerotaxy means growth on an unsupported surface, in this case promoted by a nonequilibrium plasma. The key to narrow size distributions is that the NPA mechanism is based upon surface growth, as opposed to coagulation mechanisms that result in broad size distributions. The NPA process converts the Ga aerosol into GaN NCs within 10–100 ms of residence time. The mechanism involves non-thermal vaporization of the source Ga aerosol, which is followed by nucleation and reaction with the excited N₂ species in the plasma. Particles can be made to be either hollow or solid. Solid NCs were found to be photoluminescent. Large NCs emitted photons at a peak wavelength near the bulk band-gap transition. Tuning the size to be smaller than 7 nm average diameter led to a blueshifted photoluminescence. Inline processing of these bare GaN NCs into porous films by supersonic impact deposition is demonstrated. Moving beyond the specific example of GaN, the NPA mechanism is general and can be extended to many other binary, ternary or doped semiconductors.

Keywords: gallium nitride, low temperature plasma, aerotaxy, nanocrystals, aerosol

Supplementary material for this article is available online

(Some figures may appear in colour only in the online journal)

1. Introduction

III–V nitride semiconductors are an important family of materials for applications in optoelectronics due to their band gaps that span between 0.65 to 6eV [1, 2]. Gallium nitride (GaN) is the most-studied binary compound of the III–V nitrides. An attractive feature of GaN is its large direct bandgap between 3.2 and 3.4eV depending on the crystal structure, which allows LEDs and laser diodes that operate at near ultraviolet

(UV) wavelengths. Moreover, GaN has high thermal stability, high thermal conductivity, and relatively high charge carrier mobility and breakdown field strength. It is therefore seen as a promising material in power electronics [3, 4]. Furthermore, GaN is resistant to radiation-damage [5], it is chemically stable [6] and non-toxic [7]. Such favorable properties extend the use of GaN to biomedical materials [8–11]. Due to the wide range of applications, an intense effort focused on developing methods of synthesizing GaN has been conducted over

the last three decades. Hydride vapor phase epitaxy, chemical vapor deposition and molecular beam epitaxy have become the major methods of making thin films of GaN, which is the most common form of the material [12, 13].

Synthesis of high quality GaN NCs would open up possibilities for additional applications of the semiconductor. First of all, quantum-confined crystals can extend the emission range of LEDs and laser diodes deeper into the UV, to wavelengths less than 400 nm. The estimated value of the exciton Bohr radius of GaN is approximately 3-4nm [14-16]. The ability to make GaN NCs with similar or smaller sizes would allow manufacturing of UV phosphors with tunable emission by utilizing quantum confinement. Furthermore, deposition, self-assembly and printing of GaN NCs into solid GaN structures may allow smaller optoelectronic devices [17-21]. On the other hand, particles that are larger than the exciton Bohr radius could be used for growing porous or randomly structured films comprised of GaN NCs. GaN NCs have a relatively high index of refraction (an average value of 2.4 across the visible spectrum) and are almost completely transparent to visible light when free of defects and impurities. Therefore, films comprised of high quality GaN NCs can have unique applications in photonics [22], lasing [23] and photocatalysis [24-26]. Moreover, high surface activity of GaN NCs can be utilized for fast-response gas sensors [27].

The synthesis of GaN NCs is still an active area of research. Previously, both liquid phase and gas phase methods of synthesis have been employed. Liquid phase methods generally rely on metathesis or thermolysis reactions [28]. Unlike II-VI compounds, early methods [29-33] of GaN NC synthesis in the liquid phase suffered from either poor crystallinity, poor size control, highly polydisperse size distributions or low chemical purity. The major reasons for this contrast include the covalent nature of the nitrogen bonds, compared to the relatively ionic chalcogenide bonds. Moreover, the relatively high crystallization temperature of GaN requires liquid-phase methods to employ solvents with high boiling temperature. However, very recently Choi et al succeeded in synthesizing size controlled GaN NCs with tunable photonic properties [34]. On the other hand, few gas-phase methods of GaN synthesis have been reported in the literature. These studies involved heating powders of Ga, Ga₂O₃ or organometallic Ga precursors in the presence of ammonia [35–38], pulsed laser ablation from existing bulk GaN or Ga metal [39-41], and plasma synthesis from metallic Ga or organometallic Ga precursors [42-45]. Some of the major drawbacks of these methods are the formation of large aggregates, poor size control and the necessity to use post-synthesis annealing to improve crystallinity and/or to tune stoichiometry.

In this study, we report a single step gas-phase synthesis method capable of continuously producing high quality GaN NCs that are free-standing, have no organic surface ligands, and are chemically pure, by using a nonequilibrium plasma (NEP). In the last two decades, NEPs operated in the pressure range from 1 to 10 Torr have been used successfully to produce NCs of group IV semiconductors [46, 47], metal nitrides [48, 49], phosphides [50], sulfides [51], oxides [52] and metals [53]. The general approach in previous work involves feeding the relevant organometallic precursors and

hydrides (if available) into the NEP, wherein the precursors decompose and lead to the nucleation and growth of NCs. In contrast, the method described here employs a metallic Ga aerosol and gaseous N2 as precursors, thus avoiding the need for pyrophoric and toxic chemicals. An aerosol of Ga, termed the source aerosol, is generated by evaporation-condensation and the NEP subsequently serves as the reaction environment, wherein the Ga aerosol vaporizes and reacts with excited N₂ species in the plasma to form GaN. The method is continuous, and it can provide crystalline and stoichiometric particles with controlled size, demonstrated in this study in the range from 5 to 45 nm. The plasma only contains Ga, N₂ and an inert gas, in this case Ar. Therefore, the material produced does not contain significant quantities of impurities such as C or H, which are known contaminants if hydride or organometallic precursors are used [54, 55]. These pure GaN particles are photoluminescent, and they can be made to be quantum confined, leading to photoluminescence (PL) emission at energies greater than the bulk band gap. They can be deposited in the form of porous films within the same setup right after they have been synthesized, by using a supersonic impact deposition stage. The method can be used for the synthesis of many other compound semiconductors.

We term the method of synthesis as nonequilibrium plasma aerotaxy (NPA). The method is similar to the thermal aerotaxy method used for the synthesis of phosphide and arsenide NCs and nanowires by Deppert, Samuelson and coworkers [56–58]. During the thermal aerotaxy method, a source aerosol of the group III element is generated by evaporation-condensation and a defined particle size is selected by a differential mobility analyzer. The selected portion of the aerosol is then made to react with the relevant pnictides, such as arsine or phosphine, in a high temperature environment to form the III-V semiconductor. In our system, NEP uses the whole source aerosol, and tunes the final particle size of the semiconductor NCs using the process parameters. Keeping the whole aerosol allows a throughput that is approximately 1000 times greater when compared to mobility-selected aerotaxy. Furthermore, employing a NEP reactor in place of a thermal environment has unique advantages due to the non-equilibrium features of the NEP. NCs obtain negative charges in the NEP, which prevent aggregation due to Coulombic repulsion [59]. The absence of aggregation leads to a simplified scheme of aerosol growth dynamics which primarily involve nucleation and surface growth. These mechanisms usually produce narrow size distributions [60], provided the particle size is sufficiently large.

2. Methods

2.1. Experimental setup

The setup is composed of three parts: the aerosol source, the plasma reactor and the collection section (figure 1). The whole setup was under vacuum, with pressure typically in the range from 2 to 6 Torr.

The aerosol source was a hot-filament type evaporation—condensation generator. A piece of Ga (Sigma Aldrich,

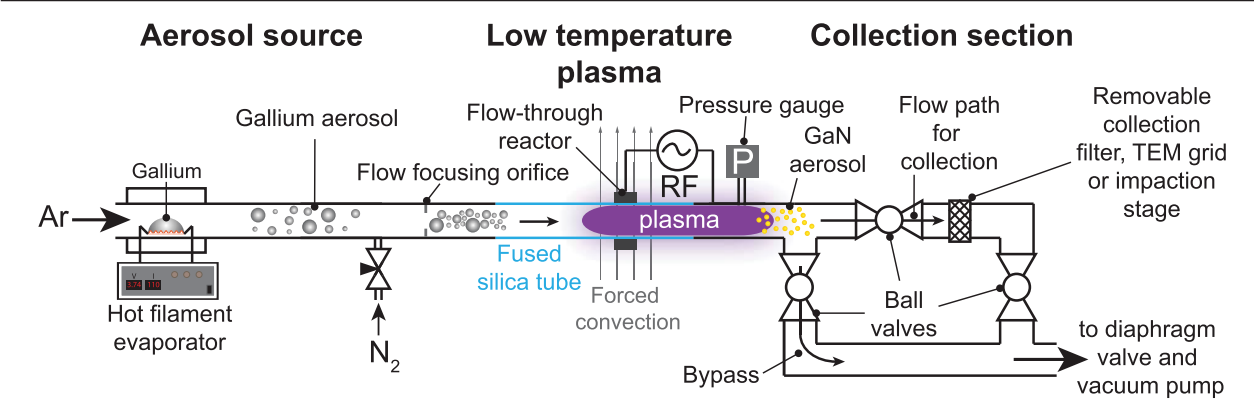


Figure 1. Experimental setup.

99.999%), usually 1 to 2 g, sat on an alumina-coated molybdenum filament. The filament was resistively heated by a DC power supply (HP 6011A). The hot Ga blob (supplementary information, figure S1 (stacks.iop.org/JPhysD/53/095201/mmedia)) produced Ga vapor, and that vapor was swept by an Ar (Praxair UHP 5.0, further purified through an alumina supported copper oxide O_2 scrubber) flow passed over the blob's surface. Thus, immediate cooling of the vapor lead to the nucleation of the Ga source aerosol. The evaporator was similar to the evaporators used in thin film deposition. However, higher gas pressures allowed faster heat-up times (approximately $200\,\mathrm{K}$ min $^{-1}$) and favored nucleation of particles. Unlike thin film deposition, each filament was used for more than 10 heating and cooling cycles, and fresh Ga was usually added after each experiment.

The mass output of the evaporator is related to the temperature of the hot Ga blob on the filament. The emission of blackbody radiation by the hot Ga blob allowed the measurement of its temperature. A fiber-coupled modular spectrometer (Ocean Optics USB2000+XR1-ES) was used for infrared thermometry. The spectrometer was calibrated for relative irradiance using a blackbody furnace (LumaSense Technologies M335). The fiber was terminated with a plano-convex lens which was aligned in such a way that through a window it viewed a 4 mm diameter spot on the hot Ga blob. The spot was smaller than the blob itself. Temperature of the blob was estimated by fitting a Wien distribution to the spectra acquired (figure S2(a)). Increasing applied power led to a sublinear increase in blob temperature (figure S2(b)). The mass output of the source (see below for measurements) increased with the temperature of the blob as expected (figure S2(c)), and it correlated closely with the calculated vapor pressure of Ga [61]. Throughout this study, Ga mass flow rates of mainly 0.3 and 0.5 mg min⁻¹ were employed, which corresponded to a temperature range of 1350 to 1450 K for the blob. The mass output of the evaporator was steady with no appreciable drift (figure S2(d)). This was due to a small increase in the temperature as the blob shrank, which compensated for the decrease in the gas-liquid contact area. Produced Ga aerosols were highly polydisperse (figure S2(e)). The tail of the distributions grew into larger particles as the mass output was increased. Aerosol mass and primary

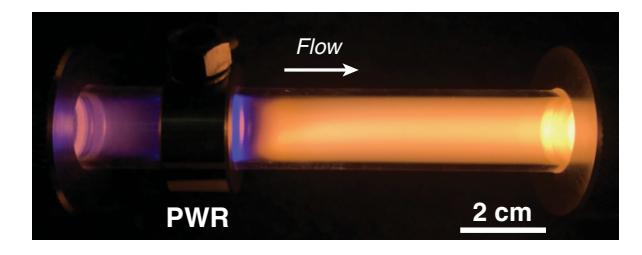


Figure 2. Flow-through plasma reactor without Ga aerosol. The pressure was 4.2 Torr. The Ar/N_2 plasma was sustained with 80 W RF power. The ring denoted by PWR is the powered electrode. No Ga particles were present.

particle number concentrations downstream of the evaporator were on the order of 1 mg $\rm m^{-3}$ and $\rm 10^{14}~m^{-3}$ respectively.

Downstream of the aerosol source, N2 (Praxair UHP 5.0, further purified through an alumina supported copper oxide O₂ scrubber) was added to the aerosol stream and the mixture was sent into a capacitively-coupled low temperature plasma reactor through a 6mm diameter orifice (figures 1 and 2). The reactor was a tubular, flow-through reactor where radiofrequency power (RF) was coupled to a stainless steel ring placed on the outside of a fused silica tube [46] (denoted as PWR in figure 2). A 13.56 MHz RF power supply (T&C Power Conversion AG0613) was used together with a matching network (T&C Power Conversion AIT600) to generate the plasma. Plasma power set at the power supply was 80 W unless otherwise noted. Reported power values are the values measured at the power supply. The power transmission efficiency of the matching network was previously measured to be approximately 65% [62]. A tube with 16 mm ID was used for experiments with a residence time greater than 20 ms. Tubes with smaller inner diameters having 10 and 7 mm were used to decrease residence times below 20 ms. The stainless-steel flange downstream of the tube was grounded. At this point, pressure was measured with a capacitive diaphragm gauge (MKS 722B Baratron). In all experiments, plasma extended primarily downstream and coupled with the grounded flange. Two viewports placed downstream of the tube were used to estimate the total length of the plasma for residence time calculations. Gas flow rates through the reactor were adjusted by mass flow controllers (MKS G-Series). Mass

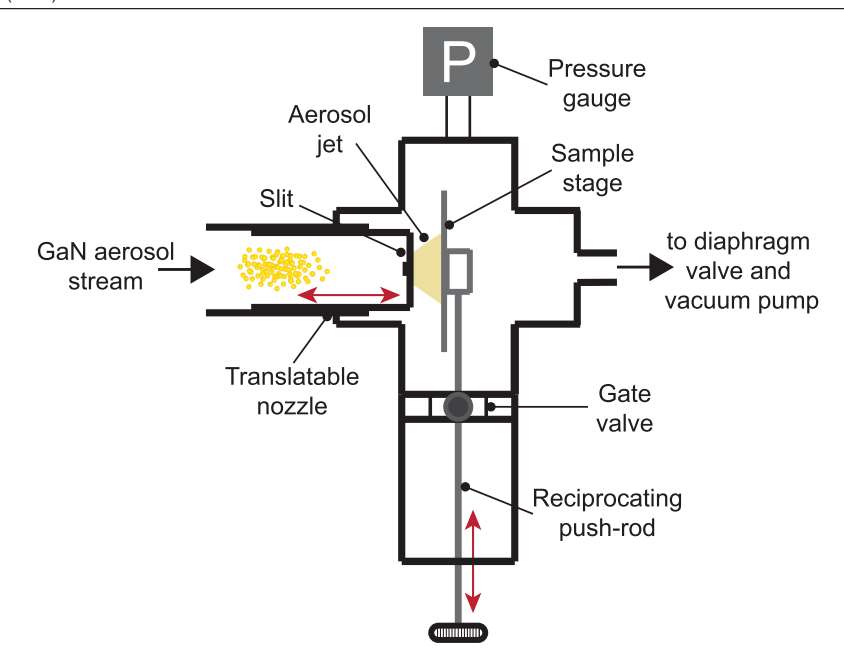


Figure 3. Schematic of the impaction apparatus. The apparatus was only used for deposition of thin films comprised of GaN NCs.

flow rates were in the range from 100 to $600 \, \text{sccm}$ for Ar and 4 to 24 sccm for N_2 . Total mass flow rates were adjusted to obtain the desired residence time. The Ar: N_2 ratio was 25:1 and the reactor was cooled with two fans.

By diverting the flow from a bypass line into a collection section, synthesized NCs were deposited on removable 400 mesh stainless steel filters and on vertically suspended lacey carbon TEM grids. The filters were weighed, and the aerosol mass flow rates were calculated. Such measurements were used to tune the output of the evaporator. In the text, only the measured mass flow rates are reported. The collection efficiency of the mesh filters was estimated by placing two filters back-to-back, separated by 8 cm. The collection efficiency measured in this way was 50%. Thus, the actual mass flow rates were 2 times greater than the reported value. The effluent from the collection section passed through a diaphragm valve that was adjusted to control the pressure in the setup, before passing into a rotary vane vacuum pump.

As a proof of concept for making GaN NC films, a portable impaction stage was inserted into the collection section (figure 3). The aerosol stream coming from the plasma was sent into a 10 mm long rectangular nozzle with dimensions of 1.2×20 mm. The pressure ratio across the nozzle, measured by a second capacitive diaphragm gauge, was approximately 4.2. NCs reach sonic velocities within the nozzle [63] and just downstream of the nozzle the aerosol beam impacts on the substrate with velocities on the order of hundreds of m s⁻¹ [64]. The NCs were deposited on Si substrates that were moved back and forth through the beam in a reciprocating motion.

2.2. Transmission electron microscopy (TEM)

Most of the imaging of the collected particles was done by using a thermal emission microscope with a LaB₆ filament

operating at 200 kV accelerating voltage (JEOL JEM-2000 FX). TEM images were used to extract the aerosol frequency distributions. By using ImageJ software, particle sizes were measured by drawing ovals that encapsulated the particles, and the diameter of the area-equivalent circle was taken as the particle size. A minimum of 200 particles were counted for samples that had a mean size larger than 10 nm. For smaller sizes, up to 1000 particles were counted. High resolution TEM (HRTEM) was conducted with a field emission scanning microscope (JEOL JEM-2100F). The same microscope was used for energy-dispersive x-ray spectrometry (EDXS) (Bruker XFlash 6T).

2.3. Powder characterization

Part of the powder collected on the filters was scraped off and characterized in its dry form. The production rate of GaN NC was in the range from 5 to 50 mg h⁻¹. Powders were subjected to x-ray diffraction (XRD) on a miscut silicon wafer with a low background signal (Bruker d8 Advance). Fourier transform infrared (FTIR) spectroscopy was conducted to characterize the surface of the particles (Thermo Scientific Nicolet 470). An attenuated total reflectance tool with a Ge crystal was employed. Spectra were corrected for the depth of penetration.

Three methods were used to determine the stoichiometry of the powders. First, EDXS was conducted with a scanning electron microscope (SEM, JEOL JSM-7001 LVF, equipped with Oxford Aztec Live X-Max EDXS detector). Secondly, thermogravimetric analysis (TGA) was utilized to estimate the Ga:N ratio by measuring the weight gain during oxidation (TA Instruments Q5000). Ceramic pans were used, and air was selected as the oxidizer during TGA. And finally, x-ray photoelectron spectroscopy (XPS) was employed. The

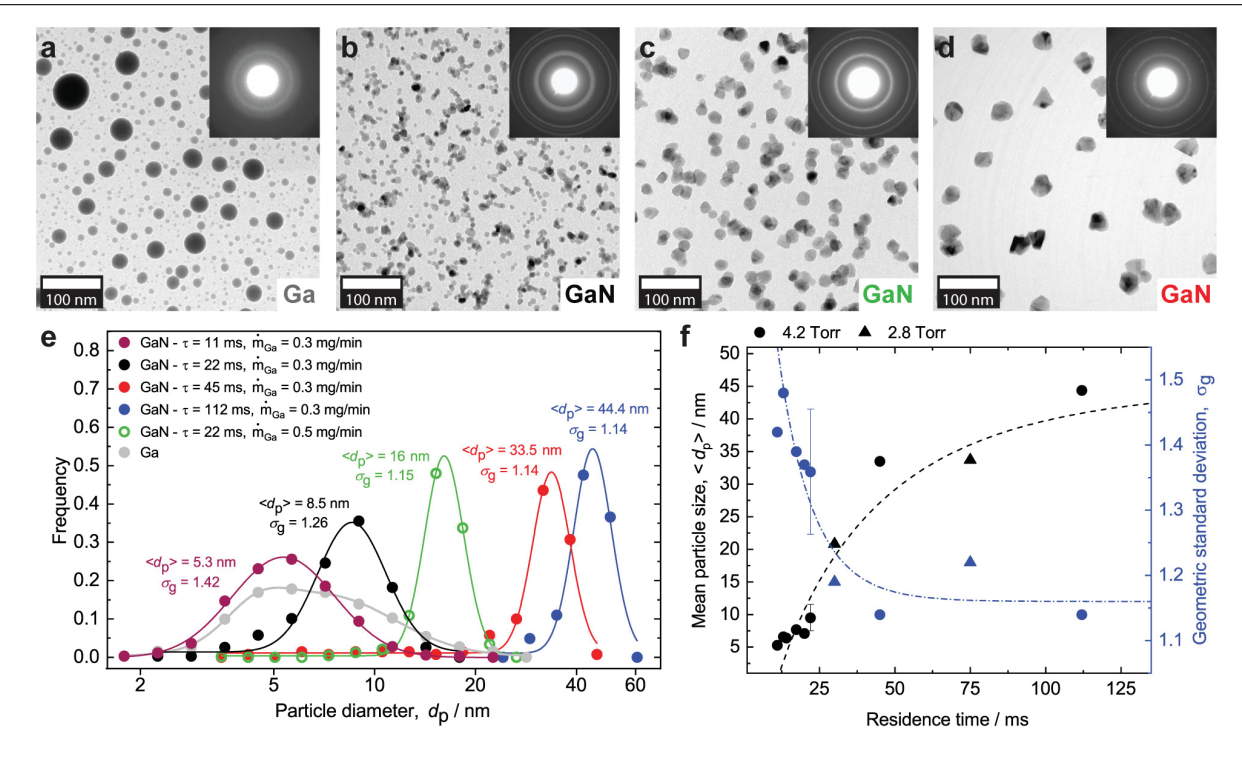


Figure 4. TEM images and size distributions. (a) Gallium aerosol produced by the hot-filament evaporator when the mass flow rate was 0.3 mg min⁻¹. (b)–(d) GaN particles of different sizes. (e) Ga and GaN size distributions obtained at 4.2 Torr pressure and at 80 W applied plasma power. The size distributions shown with circular, triangular and diamond markers belong to the aerosols shown in (b)–(d), respectively. (f) Mean particle size and geometric standard deviation as a function of residence time at two different pressures. The dashed curves are guides to the eye.

spectrometer (Physical Electronics 5000 Versa Probe II) had an Al K α source.

After the dry portion of the powder had been scraped off, the remaining portion of the powder was recovered by placing the filter in either methanol (Sigma Aldrich, 99.9%) or dimethyl sulfoxide (DMSO, Sigma Aldrich, 99.5%), and subsequently sonicating it to generate a dispersion. Absorbance spectroscopy in the UV and visible range (UV–VIS) was conducted (Shimadzu UV-1800) and the photoluminescence (PL) of the samples was measured using a fluorimeter equipped with a Xenon lamp (Shimadzu RF-6000). Concentrations of NC suspensions were typically 0.1 mg ml⁻¹. Dynamic light scattering (DLS) was utilized to estimate the aggregate sizes in solution (Malvern Zetasizer Nano ZS).

2.4. Film characterization

Films deposited on silicon wafers were characterized by SEM to obtain the film thickness. An x-ray fluorescence spectrometer (XRF, Spectro Midex MID01) was calibrated by using solid GaN templates (MTI Corporation, 500 nm thickness, on Si) with measured thickness to estimate the porosity of the films.

2.5. Plasma characterization

Optical emission spectroscopy (OES) was conducted with the same spectrometer used for the temperature measurement of

the Ga blob. Background gas temperature was measured with a fiber optic temperature probe (OptoTemp 2000 Super Probe, Micromaterials Inc) that operates on the basis of fluorescence decay of a phosphor located at the tip of the probe [65, 66]. Such probes have been demonstrated to be an adequate tool for measuring the background temperature in low temperature RF plasmas [62]. The fiber optic probe was inserted 1.5 cm downstream of the powered electrode by using a glass tube with a sidearm. Plasma parameters were measured by using a double Langmuir Probe (Impedans LTD, Dublin, Ireland). Platinum tips of 5.8 mm length and 0.37 mm diameter were used. Similar to the temperature probe, the Langmuir probe was inserted by using a tube with a side arm. The method of analysis of I–V curves is outlined in the supplementary information.

3. Results and discussion

3.1. NC size control and morphology

Upon sending the polydispersed spherical droplets of Ga (figure 4(a)) along with N_2 into the NEP, NCs of different shapes and sizes were produced. Selective area electron diffraction (SAED, figures 4(a)–(d) insets) immediately revealed that these NCs were crystalline GaN.

The NPA method is capable of providing good size control in the synthesis of GaN NCs (figure 4(e)). Extensive TEM investigations on collected NCs showed that one of the most

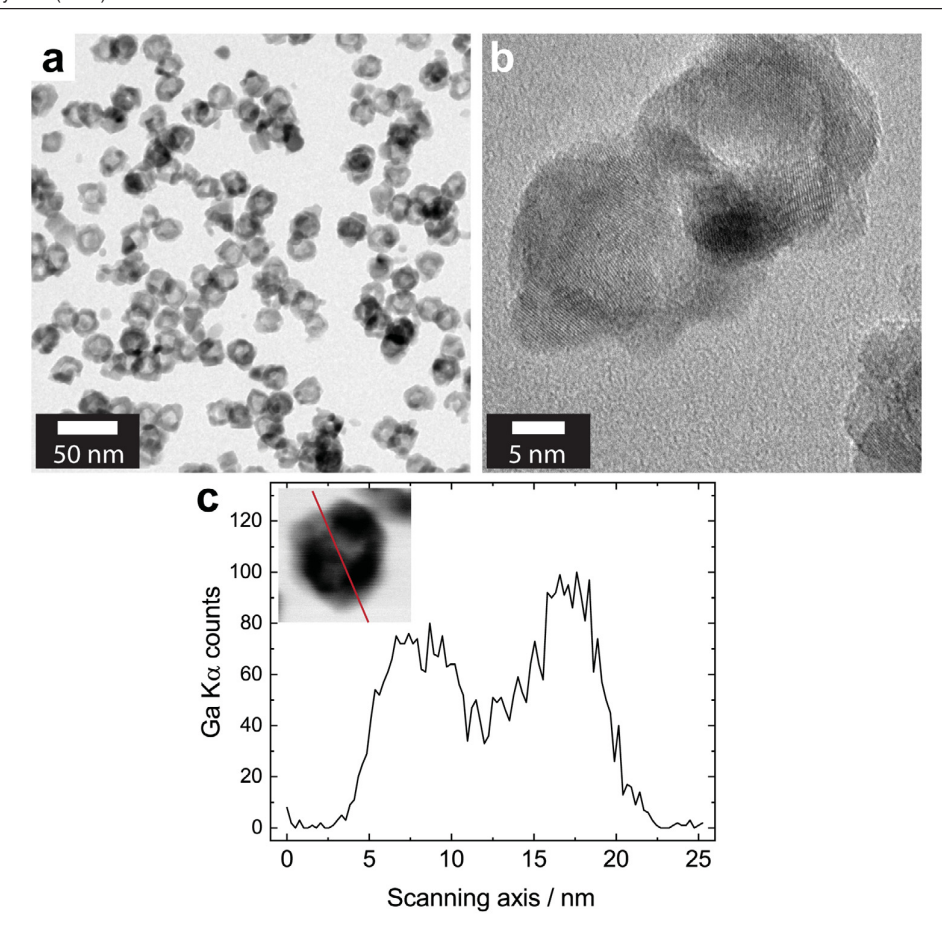


Figure 5. Hollow particles. (a) Hollow particles synthesized at 6 Torr (see figure S6 for details) (b) HRTEM image of two superposed hollow particles. (c) EDXS line scan across a hollow particle.

straightforward process parameters for size control is the residence time in the plasma. As the residence time in the plasma increased, the mean particle diameter, $\langle d_p \rangle$, also increased; and the size distributions became narrower. For residence times longer than 45 ms, size distributions approached to the definition of a monodisperse size distribution: $\sigma_g \leqslant 1.1$, where σ_g is the geometric standard deviation. The fitted curves given in figure 4(e) are lognormal distributions.

Interestingly, the Ga source aerosol was found to be highly polydispersed at all of the aerosol mass flow rates employed (figure S2(e)), and yet, it was possible to synthesize GaN NCs with much narrower size distributions. Furthermore, in some cases the GaN NCs were smaller than the Ga source aerosol, and in other cases they were larger than the Ga source aerosol. Figure 4(f) summarizes the trends in particle size and geometric standard distribution obtained during experiments conducted at a pressure of 4.2 Torr with 0.3 mg min⁻¹ mass input. A limited number of experiments conducted at a slightly lower pressure of 2.8 Torr indicated that the effect of pressure on $\langle d_p \rangle$ and σ_g was modest over that range. NCs smaller than 10 nm appeared to be approximately spherical in shape (figure 4(b)), however, larger particles were found to be faceted (figures 4(c) and (d)).

NC size distributions could also be tuned by changing the Ga aerosol mass flow into the reactor. Increasing the mass

input led to larger NCs. For example, at a residence time of 22 ms, ramping the Ga feed rate from 0.3 mg min⁻¹ to 0.5 mg min⁻¹ approximately doubled the average diameter (figure 4(e)). After scanning residence times between 10–150 ms and mass inputs between 0.15 to 1.5 mg min⁻¹, the maximum $\langle d_p \rangle$ that could be obtained was found to be approximately 45 nm. Increasing the Ga mass flow beyond 0.5 mg min⁻¹ resulted in a higher GaN throughput, but $\langle d_p \rangle$ and σ_g remained approximately constant (data not shown). In all experiments, the mass concentration and primary particle number concentration of the GaN aerosol were on the order of 0.1 mg m⁻³ and 10^{13} m⁻³ respectively.

An interesting feature of the NPA method is that it is capable of making monodisperse and hollow particles (figures 5 and S4). HRTEM imaging revealed that hollow particles had a polycrystalline shell (figure 5(b)). The hollowness of the core was demonstrated by EDXS. Line scans across hollow particles were conducted and the Ga $K\alpha$ counts were found to dip in the middle of the particle, indicating a hollow core (figure 5(c)). These particles were found to form under higher pressures, and at lower powers (figure S5). The emergence of hollow morphology, and the conditions at which these particles form, provide insights into the formation mechanism of GaN NCs in the NPA process (vide infra).

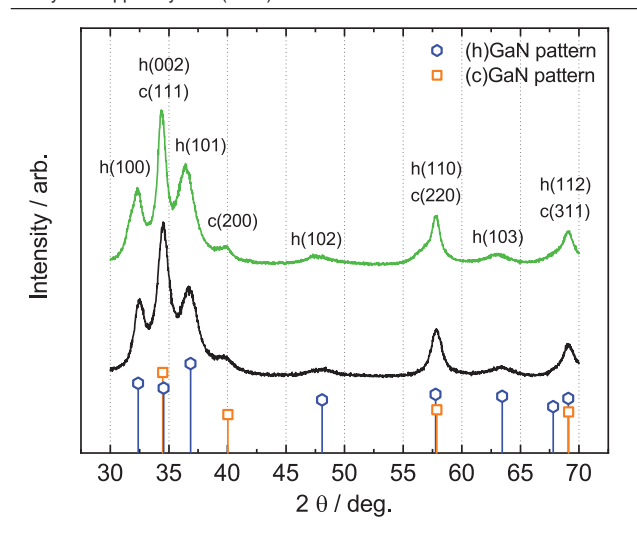


Figure 6. XRD spectra. The lower curve corresponds to the sample in figure 4(b), which is also in figure 4(e) marked by black circles. The upper curve corresponds to the sample in figure 4(c), which is also in figure 4(e) marked by green triangles.

3.2. Crystallinity and stoichiometry

XRD analysis showed that all particles synthesized with plasma powers larger than 40 W were crystalline, confirming SAED results. Both XRD and SAED indicate that the product was a mixture of cubic and hexagonal GaN (figures 6 and S6(a)). No presence of metallic or oxidized Ga was detected. Rietveld refinement and quantitative phase analysis suggested that the phase composition was from 50 to 66% hexagonal, balance cubic (e.g. figure S7). Using the Scherrer equation on the diffraction peaks of the black lower curve in figure 6, which corresponds to the sample with black circle markers in figure 4(e), yields a crystallite size of 8 nm. For that sample comprised of small particles, the crystallite size from XRD was very close to the average NC diameter measured by TEM, indicating the particles were single crystals. However, the upper green curve in figure 6 that corresponds to the sample with green triangle markers in figure 4(e) yields a crystallite size of 5-9 nm depending on the peak used for analysis, which is significantly smaller than the diameter measured by TEM. Therefore, for these larger particles, the NCs were polycrystalline. In general, NCs larger than 15 nm were found to be polycrystalline, and smaller particles were found to have a single crystallographic orientation. Comparison of the SAED data to XRD patterns suggests that preferential orientation effects were absent from the XRD patterns and the particles were approximately spherical (figure S6(b)–(d)).

ATR-FTIR spectroscopy (figure S8) showed that the surface of the GaN NCs were populated by physisorbed water and N–H bonds. A sharp peak for the phonons of GaN at 580 cm⁻¹ is consistent with the high level of crystallinity revealed by SAED and XRD. The feint shoulder at 715 cm⁻¹ next to the phonon peak is associated with the Ga–O–Ga center [67], likely coming from a native surface oxide. No presence of the features belonging to nitrogen deficiencies or antisite defects were found [68]. It was reported that over the course

of a year under ambient atmosphere, GaN NCs transform into gallium oxy hydroxide (GaOOH) [69]. For our samples, after two months, the transformation to GaOOH became visible in FTIR spectra due to the appearance of a doublet at 947 and $1014\,\mathrm{cm}^{-1}$ that corresponds to Ga–OH [70].

The Ga:N ratio of the NCs was found to be close to 1:1. SEM-EDXS and TGA gave similar results, and XPS qualitatively verified the measurements. None of the listed characterization techniques are ideal for analyzing GaN nanopowders, thus all three were employed to reach a reliable conclusion. EDXS was conducted and multiple measurements on multiple samples indicated a Ga:N ratio of 1.0 ± 0.2 (figure S9). Although the measured stoichiometry had the desired value, the spread in measurements was relatively large. The relatively large spread can be due to the common errors in the quantification of light elements such as nitrogen in EDXS, or from the rough texture of the powder. TGA was used as a second method to confirm EDXS results. It was assumed that all particles were essentially comprised of Ga and N with arbitrary Ga:N ratio, and the amount of the initially present oxide on the surface was omitted. It was further assumed that all Ga atoms end up forming Ga₂O₃. Thus, the percent change in sample weight allowed the calculation of the Ga:N ratio. Results indicated that the stoichiometry of powders was very close to 1:1 (figure S10).

XPS analysis qualitatively confirmed that the product was GaN and no free Ga was present. In principle, XPS can be quantitative by either using the empirical elemental sensitivity factors or by using a reference material. However, quantitative analysis was hindered by the overlap of the Ga Auger transitions (L₂M₄₅M₄₅ and L₃M₄₅M₄₅) with the N 1s transition, which is inevitable when an Al K α x-ray source is used. Furthermore, using a reference material, in this case single crystal (SC) GaN, was found to have its own difficulties. Sputtering was required to expose the bulk of the reference material and to detect the N 1s transition, and thus the wellknown preferential sputtering of N in nitrides [71, 72] made quantification unreliable. Instead of having a quantitative analysis, the XPS spectra of GaN NCs were compared qualitatively with the spectrum of the SC. The SC was sputtered for 1 min under 2 keV Ar⁺ beam. The survey spectra of the NCs and of the SC looked very similar (figure S11(a)) and both had peaks corresponding to Ga and N. The only difference was the O and C detected in the NCs. Oxygen 1s signal was expected to be due to the surface oxide, and C 1s signal was due to adventitious carbon. These features were always present on the NCs even when sputtering was employed, because the surface of some of the NCs was always exposed during analysis. Higher resolution spectra gathered from the NCs and SC of the Ga 3d and N 1s transitions were also found to be similar. The Ga 3d peak for NCs was initially positioned at 18.8 eV due possibly to some sub-oxide or oxynitride on the surface (figure S11(b)). Upon sputtering, the peak corresponding to GaN appeared at 17.3 eV, which was also seen in the GaN SC (figure S11(c)). Similar correspondence between the NCs and SC were found for the N 1s and Ga Auger peaks between 388–400 eV. Sputtering of NCs led to an increase in the intensity of Ga Auger peaks, especially at 392 eV (figure S11(d)),

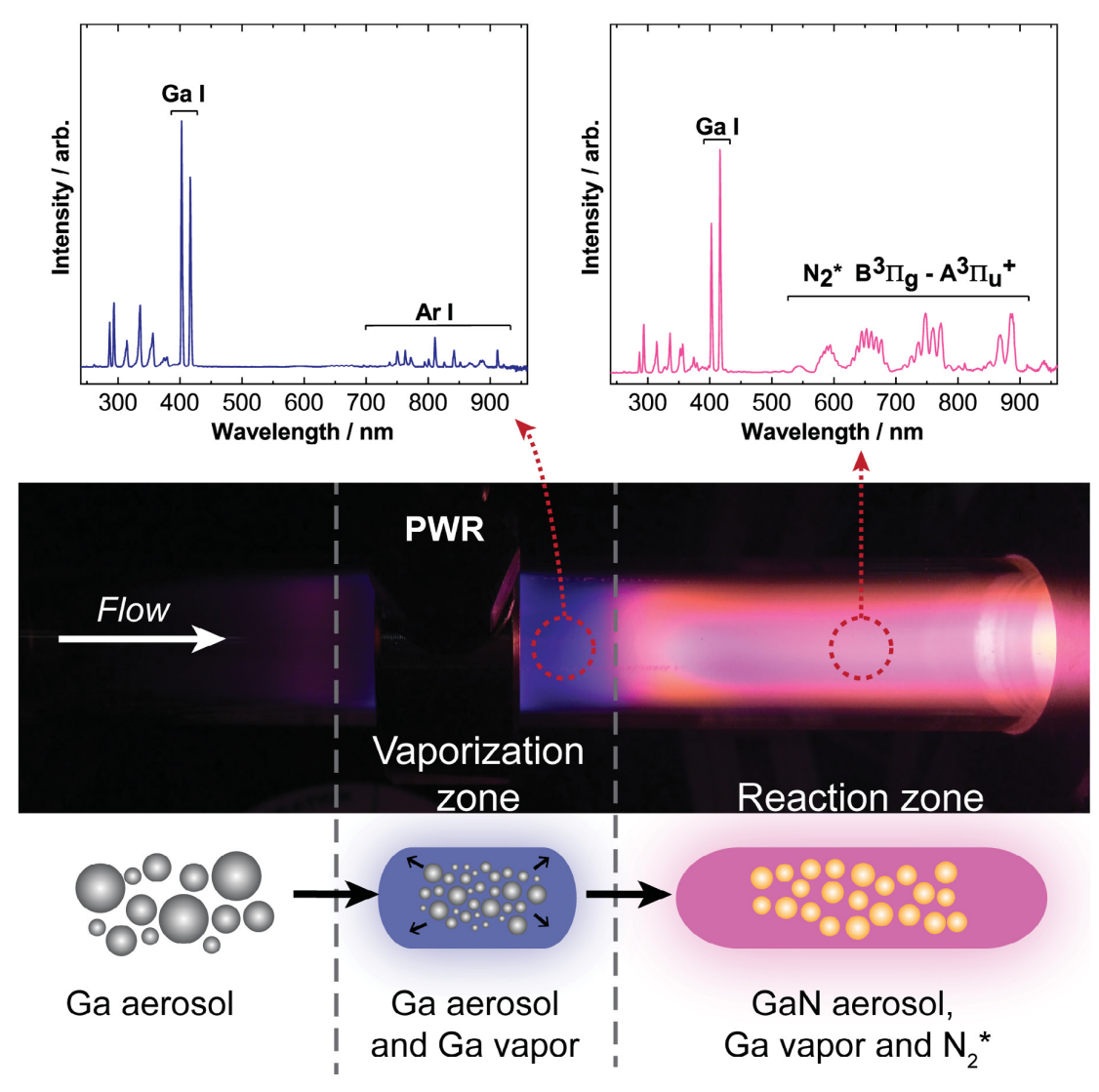


Figure 7. GaN formation mechanism in the NPA process. The plots on the top represent the plasma emission collected from the spots shown by red dashed circles. The photograph shows the reactor during GaN synthesis.

indicating preferential sputtering of N. The same shoulder was also observed for the SC (figure S11(e)).

Complimentary to the aforementioned evaluations of stoichiometry, the color of the synthesized powder can be used to assess the quality of the NCs in terms of Ga:N ratio, defects, and oxygen impurities. Dark brown color in GaN has been associated with defects, oxygen impurities and N deficiency [73, 74]. Since GaN single crystals are completely transparent in the visible region of the spectrum owing to their large band gap, perfect stoichiometric powder is expected to be white due to scattering. Most of the samples characterized in this study either had a pale-yellow color or they were white (figure S12), indicating that the stoichiometry of the NCs was close to 1:1 and defect densities were low.

3.3. Growth mechanisms and the effects of operation parameters on size, crystallinity and stoichiometry

The evidence is consistent with a synthesis mechanism that involves vaporization of the Ga source aerosol in the vicinity of the powered RF electrode, followed by reaction of that Ga vapor with excited N_2 species further downstream to nucleate and grow GaN NCs by an aerotaxy process. A schematic of the mechanism is presented in figure 7. In the vaporization zone near the powered electrode, only excited atomic gallium and excited argon were observed in the emission spectrum from the plasma, while further downstream, emission from excited N_2 molecules was also observed (figure 7). Trends in the size distribution and morphology of the GaN NCs compared to the Ga source aerosol are also consistent with the mechanism depicted in figure 7.

To infer the growth mechanism from the results of NC size control experiments, one should first know whether the particles sampled on TEM grids actually represent the produced GaN aerosol. In other words, the collection efficiency of the TEM grid should be known as a function of particle size. Detailed calculations using computational fluid dynamics (CFD, figures S13–15) indicated that the main mechanism of deposition is diffusion and the capture efficiencies of GaN

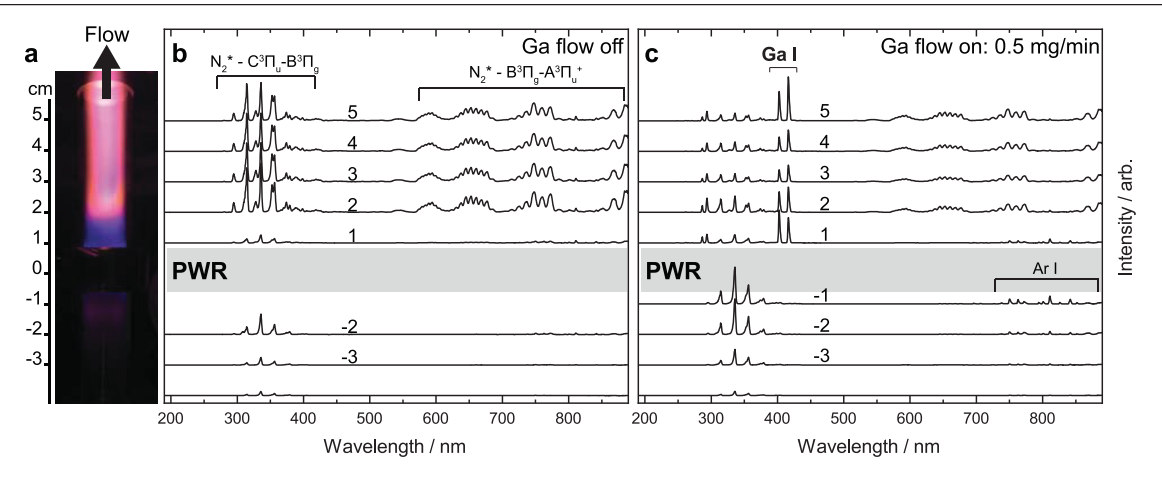


Figure 8. Optical emission spectroscopy. (a) Plasma with Ga aerosol at 80 W and at 4.2 Torr pressure. Ar: $N_2 = 25$ with a total flow of 520 sccm. (b) Emission spectra as a function of axial position when there was no Ga aerosol flow into the plasma. The axial position at 0 cm corresponds to the powered RF electrode. (c) Emission spectra as a function of axial position when there was 0.5 mg min⁻¹ Ga aerosol flow into the plasma.

NCs synthesized are similar within the ranges of sizes explored in this study (figure S16). Therefore, the size distributions obtained from particles deposited on the TEM grids during synthesis closely represent the actual particle size distributions of the as-produced aerosol (figure S17). The result partially stems from the fact that the size distributions of GaN NCs are usually narrow. However, the Ga source aerosol was found to have a much larger mean size and a broader size distribution that spanned across more than a decade in size, after correcting for sampling bias. Interestingly, the highly polydispersed source aerosol vanished in the plasma, and a GaN aerosol with a much narrower size distribution was obtained in all cases.

Such a polydisperse-to-monodisperse transformation was demonstrated in NEPs before. In a previous study, polydisperse Bi particles were sent into a similar Ar NEP and they were found to transform into monodisperse aerosols [60]. Bi vapor was detected in the plasma, and the authors argued that the aerosol almost completely vaporized in a zone in the vicinity of the powered electrode. That zone had an higher ion density, which is responsible for non-thermal heating the particles mainly due to ion-electron recombination on particles' surface [62, 75-77]. Downstream of this intense zone where the aerosol vaporized, a new monodisperse aerosol formed by nucleation and condensation. The similarity of the disappearance of the Ga source aerosols and the formation of GaN NCs with a narrower size distribution and with smaller mean sizes in the experiments reported here suggest that Ga droplets should shrink down to very small sizes, possibly vaporizing completely, in the plasma before reacting with nitrogen.

Results from OES suggest that the Ga aerosol vaporizes in the NEP, in a way that is very much similar to the Bi aerosol example cited above (figure 8). With no Ga aerosol present, the Ar/N₂ plasma produced feint Ar I emission [78] and emission from the second positive system of molecular N₂ ($C^3\Pi_uB^3\Pi_g$) in the vicinity of the powered electrode (figures 2 and 8(b)), due to resonant energy transfer between Ar metastables N₂. Downstream of the powered electrode, emission was primarily dominated by the first positive system of

molecular N_2 emission ($B^3\Pi_g - A^3\Pi_u^+$), which could be seen as a bright orange glow by naked eye (figure 2). When Ga aerosol was sent into the plasma, bright blue Ga I emission [78] was observed just downstream of the powered electrode, along with a more intense Ar I emission (figures 7, 8(a) and (c)). Adding Ga quenched the Ar metastables, and thus the emission from the second positive system of N_2 was of significantly lesser intensity downstream of the powered electrode. However, emission from the first positive system was still quite distinct, likely caused by lower excitation energies of this system and consequent direct electron excitation. Ga I emission was present throughout the plasma downstream of the powered electrode.

It should be mentioned that the measured background temperatures ($<400\,\mathrm{K}$) were much lower than the temperatures necessary to vaporize the Ga aerosol (figure S18). Therefore, the vaporization mechanism was non-thermal in nature and was expected to occur primarily due to ion and electron bombardment. An unexpected aspect of the Ga I and molecular N_2 emission was that these features were found to fluctuate with a period on the order of minutes (figure S19). Although the reason for this effect is unidentified, it could have been caused by particle trapping in the plasma, which was shown to follow periodic trends on a similar time scale [79].

Vaporization of Ga is expected to occur predominantly in the vicinity of the powered electrode. Previous double Langmuir probe measurements in Ar plasma indicated a higher ion density inside and nearby the powered electrode [62], which is expected to cause higher particle temperatures and vaporization rates [60, 62]. In the case of the Ar/N₂ plasma employed in this study, ion densities were measured 2 cm downstream of the powered electrode. At this location, the ion density of the pristine plasma with no Ga source aerosol was found to be $1.78 \times 10^{18} \, \mathrm{m}^{-3}$ at $4.2 \, \mathrm{Torr}$. The ion density inside the powered electrode is expected to be 2 to 3 times larger than this measured ion density [62]. In the presence of an aerosol and metal vapor, common expectation is a decrease in electron temperature and an increase in ion density [80, 81].

With the source aerosol being sent into the plasma, double Langmuir probe measurements were done nearby the zone with intense bright blue Ga I emission. In accordance with the expectations, electron temperature dropped from 2.74 eV to 2.30 eV, and ion density increased to $2.05 \times 10^{18} \text{ m}^{-3}$ (figure S20 and table S1). A major problem encountered while doing Langmuir probe measurements was contamination of the probe tips. During NC synthesis, probes were coated with a form of GaN, which formed an insulating layer. An insulating layer is known for erroneously increasing the measured electron temperature [82], opposite to what was observed in our measurements. However, when the coated tips were used to measure the parameters of the pristine plasma, an even lower electron temperature, 2.01 eV, was obtained, but ion density of the pristine plasma was recovered (table S1). Cleaning the probe tips with a fine sandpaper allowed us to re-measure similar values as the pristine plasma without Ga. Although measurements provided some insight, it is clear that the use of a double Langmuir probe is hindered by the contamination of the tips during NPA. Therefore, other diagnostic methods are necessary to assess the effect of the source aerosol and metal vapor on the plasma parameters. Since the plasma parameters determine the particle charge and rates of ion bombardment, the extent of vaporization of the source aerosol is expected to be dependent on the parameters of the dusty plasma. Hence, the source aerosol and the plasma are expected to be strongly coupled. Nevertheless, a qualitative observation was made on the extent of vaporization of the source aerosol. It was observed that the zone emitting bright blue Ga I emission became longer when applied power was increased (figure S21). As power was increased, yield decreased due to more Ga vapor being lost to the walls just nearby the powered electrode. At low powers, however, Ga did not vaporize as much. Moreover, at low powers the N2 glow was weaker, and the reaction happening downstream was incomplete (vide infra). Therefore, an optimum intermediate power, e.g. 80 W, was required to obtain both acceptable yield and high quality GaN NCs.

The reaction between Ga clusters, Ga vapor and excited N₂ molecules is hypothesized to occur downstream of the powered electrode. That hypothesis is supported by the presence of both Ga I emission and molecular N2 emission in that region (figure 8). Therefore, the Ga-vapor rich plasma downstream of the powered electrode, in which excited nitrogen species were also present, is considered as the reaction zone and the length of that plasma was used to estimate the residence times reported in this study. The Ga I emission was likely coming from either a minute quantity of Ga aerosol that was still vaporizing, or from newly formed GaN. However, the increase in size with longer residence time suggests that some GaN particles disappeared throughout the reactor and growth of larger particles was more favorable than smaller particles. While the mechanism of this selection is unclear, it could be due a portion of particles having a higher temperature due to charge fluctuations or some of them being smaller in size [62], or due to differences in local ion density.

Formation of hollow particles suggests that the growth mechanism of the GaN NCs has to involve the condensation of

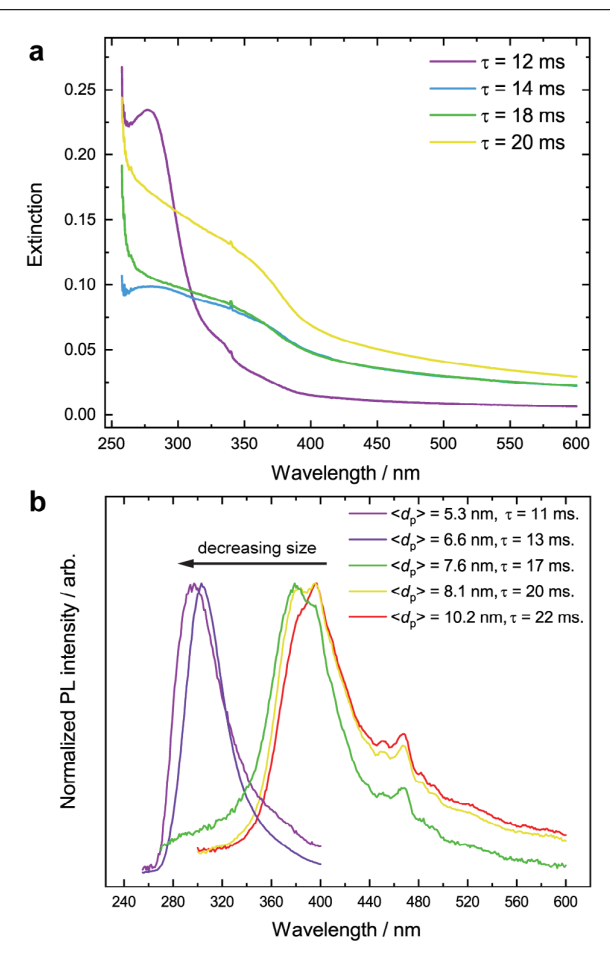


Figure 9. Photonic properties. (a) UV–VIS absorption spectra of particles obtained at different residence times τ . (b) PL spectra of particles with different mean sizes obtained at different residence times. An excitation wavelength of 210 nm was used.

Ga and surface reaction of excited N₂ species on Ga droplets and GaN clusters. A hypothesis is given as follows. At lower ion densities, i.e. low power and/or higher pressure [62], the Ga aerosol vaporizes less, and the Ga droplet sizes entering the reaction zone are fairly large. The N2 glow is also expected to be weak, however, some excited N₂ species diffuse into the Ga droplets and GaN phase nucleates to some extent. During this process with large Ga droplets and slow rates, the reaction is incomplete as many Ga particles do not get converted into GaN and only a few hollow particles form (figure S5). As power is increased, more hollow particles are formed (figure S4) due to radial volume expansion [83] upon conversion of Ga into GaN, since the molar specific volume of GaN is 20% larger than Ga. At even higher powers, and consequent higher particle temperatures, more facile solid-state transport and particle vaporization result in solid particles.

3.4. Photonic properties

Explicit control on the particle size distributions of high quality GaN NCs allows the NPA method to provide control over photonic properties. Absorption and photoluminescence spectroscopy performed on colloidal suspensions of GaN NCs was used to investigate the effect of particle size on photonic properties. Since no organic ligands were used in this work to aid dispersion, the GaN particles tended to form large agglomerates in solution. To prevent scattering from the agglomerates as much as possible, NCs were suspended in DMSO during absorption spectroscopy. DMSO was selected due to its unique nanoparticle solvation capability [84], as evidenced by much smaller aggregates size (~200 nm z-average size as measured by DLS) in comparison to very large aggregates formed in methanol (500–1000nm). However, methanol was employed during PL measurements due its low absorption coefficient at UV excitation wavelengths.

UV-VIS absorption spectroscopy indicated that the smallest GaN NCs exhibited quantum confined states (figure 9(a)). As particle size was made to be smaller, the extent of scattering was decreased, and an excitonic absorption peak emerged at 280 nm.

PL measurements indicated near band-gap emission from particles that were larger than 8 nm (figure 9(b)). When excited with 210nm light, the emission profile includes a peak at 396 nm and another peak at 380 nm. With some Stokes shift, these peaks likely correspond to band gap emission of the hexagonal and cubic phases respectively. As particle size decreased below 7 nm, the PL peak abruptly shifted to 305 nm. The PL peak further blueshifted as the particles were made even smaller, demonstrating behavior consistent with quantum confinement. Apart from the long tail of the nearband gap emission and the weak emission at 468 nm for larger particles, which was likely present due to a shallow donoracceptor pair caused by defects on the surface of the particles [85], additional defect emissions, such as the common yellow emission seen in GaN thin films, were absent. Over the course of two months, particles that exhibited near-band gap PL were found to be relatively stable (figure S22). The emission intensity decreased approximately 20% each month and the 380 nm emission corresponding to hexagonal GaN became relatively stronger in comparison to the 396 nm emission from cubic GaN as time proceeded. This result indicates that the cubic phase, which is metastable, might be deteriorating faster than the thermodynamically stable hexagonal phase in methanol.

3.5. Films comprised of GaN NCs

Although the production of bare particles presents some difficulties in photonic measurements in simple NC dispersions due to aggregation and leads to their eventual conversion into GaOOH, these bare particles are in fact the desired form for films comprised of NCs. The absence of ligands is expected to lead to films with higher electrical conductivity [86, 87], and these films can be subjected to common post-processing methods for thin films, such as annealing, etching and further packaging. For porous films, supersonic impaction is a capable method of making films out of NCs, right after they have been synthesized [63]. A 900 nm porous GaN NC film was prepared as an example, and a cross sectional SEM image

of that film is presented in the supporting information (figure S23). The film was composed of particles that were relatively large, 35 nm mean diameter, when compared to particles that have previously been used to make NC films by supersonic impact deposition [63, 88]. Although the employed pressure ratio was very small, approximately 4.2, the film had surprisingly high fill fraction. The fill fraction measured by XRF was 34%. Such NC films are expected to find applications in optoelectronics and photonics.

4. Conclusions and outlook

A new gas phase synthesis method for making NCs of compound semiconductors was presented. The advantages of this new method, termed NPA, were displayed by demonstrating the synthesis of pure and bare GaN NCs. Produced GaN NCs can be made to be any desired size between 5–45 nm, and the size distributions can be made to be narrow. NCs were found to be crystalline and stoichiometric. The GaN NCs were photoluminescent with emission ranging from 300 to 400 nm.

Clarifying the growth mechanism in the NPA process is essential for improving control on particle size and reactor yield. Particle size distributions were found to be broader for the smallest NCs produced. In order to control quantum confinement effects, a quantitative understanding of the growth process is required to optimize reactor geometry and operation parameters accordingly. On the way to achieving this goal, characterization of dusty NEP, such as the one used in this study, is a challenging but crucial step that needs to be accomplished. With the plasma parameters in hand, the effect of aerosol and metal vapor on plasma properties can be identified. Furthermore, predictive models of aerosol dynamics and growth in NEP can be developed.

NPA can be extended to many other materials, involving binary, ternary and doped semiconductors. However, there are two constraints. First, the constituent metals and semi-metals must be aerosolized. If an evaporation–condensation generator is to be employed, such as the hot filament generator used in this study, then the constituent element must have sufficiently high vapor pressure. Fortunately, a large class of elements fulfill that criterion. The second constraint is that the plasma should be able to vaporize the aerosol, which is essential for size control. We believe that constraint can be satisfied with low pressure NEP.

Acknowledgments

The authors acknowledge financial support from the Army Research Office MURI grant W911NF-18-1-0240. This work was performed in part at the Nano Research Facility (NRF) and at the Institute of Materials Science and Engineering at Washington University in Saint Louis, and the authors acknowledge financial support for the use of instruments and staff assistance. The authors would like to thank Dr Dariusz Niedzwiedzki for his assistance during photoluminescence measurements and Dr Huafang Li for her help and guidance during transmission electron microscopy.

ORCID iDs

Necip B Uner https://orcid.org/0000-0002-5719-6417 Elijah Thimsen https://orcid.org/0000-0002-7619-0926

References

- [1] Vurgaftman I, Meyer J R and Ram-Mohan L R 2001 Band parameters for III–V compound semiconductors and their alloys J. Appl. Phys. 89 5815–75
- [2] Nag B R 2003 On the band gap of indium nitride *Phys. Status Solidi* b **237** R1–2
- [3] Chow T P and Tyagi R 1993 Wide bandgap compound semiconductors for superior high-voltage power devices Proc. 5th Int. Symp. on Power Semiconductor Devices and ICs pp 84–8
- [4] Pearton S J, Abernathy C R and Ren F 2006 *Gallium Nitride Processing for Electronics, Sensors, and Spintronics* (New York: Springer)
- [5] Sellin P J and Vaitkus J 2006 New materials for radiation hard semiconductor detectors *Nucl. Instrum. Methods Phys. Res.* A 557 479–89
- [6] Foster C M, Collazo R, Sitar Z and Ivanisevic A 2013 Aqueous stability of Ga- and N-polar gallium nitride Langmuir 29 216–20
- [7] Jewett S A, Makowski M S, Andrews B, Manfra M J and Ivanisevic A 2012 Gallium nitride is biocompatible and non-toxic before and after functionalization with peptides Acta Biomater. 8 728–33
- [8] Foster C M, Collazo R, Sitar Z and Ivanisevic A 2013 Cell behavior on gallium nitride surfaces: peptide affinity attachment versus covalent functionalization *Langmuir* 29 8377–84
- [9] Bain L E and Ivanisevic A 2015 Engineering the cellsemiconductor interface: a materials modification approach using II–VI and III–V semiconductor materials *Small* 11 768–80
- [10] Ismail A, Pittet P, Lu G N, Galvan J M, Giraud J Y and Balosso J 2011 In vivo dosimetric system based on gallium nitride radioluminescence Radiat. Meas. 46 1960–2
- [11] Kirste R, Rohrbaugh N, Bryan I, Bryan Z, Collazo R and Ivanisevic A 2015 Electronic biosensors based on III-nitride semiconductors Annu. Rev. Anal. Chem. 8 149–69
- [12] Strite S, Lin M E and Morkoç H 1993 Progress and prospects for GaN and the III–V nitride semiconductors *Thin Solid Films* 231 197–210
- [13] Molnar R J, Götz W, Romano L T and Johnson N M 1997 Growth of gallium nitride by hydride vapor-phase epitaxy J. Cryst. Growth 178 147–56
- [14] Leszczynski M *et al* 1996 Lattice parameters of gallium nitride *Appl. Phys. Lett.* **69** 73–5
- [15] Levinshteĭn M E, Rumyantsev S L and Shur M 2001 Properties of Advanced Semiconductor Materials: GaN, AlN, InN, BN, SiC, SiGe (New York: Wiley)
- [16] Ridley B K 1999 Quantum Processes in Semiconductors (Oxford: Clarendon)
- [17] Krinke T J, Deppert K, Magnusson M H and Fissan H 2002 Nanostructured deposition of nanoparticles from the gas phase Part. Part. Syst. Charact. 19 321–6
- [18] Fissan H, Kennedy M K, Krinke T J and Kruis F E 2003 Nanoparticles from the gas phase as building blocks for electrical devices J. Nanopart. Res. 5 299–310
- [19] Wegner K, Piseri P, Tafreshi H V and Milani P 2006 Cluster beam deposition: a tool for nanoscale science and technology J. Phys. Appl. Phys. 39 R439–59
- [20] You S, Han K, Kim H, Lee H, Woo C G, Jeong C, Nam W and Choi M 2010 High-resolution, parallel patterning of

- nanoparticles via an ion-induced focusing mask *Small* **6** 2146–52
- [21] Magnusson M H, Ohlsson B J, Björk M T, Dick K A, Borgström M T, Deppert K and Samuelson L 2014 Semiconductor nanostructures enabled by aerosol technology *Frontiers Phys.* 9 398–418
- [22] Zhong Z, Qian F, Wang D and Lieber C M 2003 Synthesis of p-type gallium nitride nanowires for electronic and photonic nanodevices *Nano Lett.* 3 343–6
- [23] Cao H, Xu J Y and Zhang D Z 2000 Spatial confinement of laser light in active random media Phys. Rev. Lett. 84 4
- [24] Maeda K, Teramura K, Saito N, Inoue Y and Domen K 2007 Photocatalytic overall water splitting on gallium nitride powder *Bull. Chem. Soc. Japan* 80 1004–10
- [25] Jung H S, Hong Y J, Li Y, Cho J, Kim Y-J and Yi G-C 2008 Photocatalysis using GaN nanowires ACS Nano 2 637–42
- [26] Kibria M G, Zhao S, Chowdhury F A, Wang Q, Nguyen H P T, Trudeau M L, Guo H and Mi Z 2014 Tuning the surface Fermi level on p-type gallium nitride nanowires for efficient overall water splitting Nat. Commun. 5 3825
- [27] Chitara B, Late D J, Krupanidhi S B and Rao C N R 2010 Room-temperature gas sensors based on gallium nitride nanoparticles Solid State Commun. 150 2053–6
- [28] Fan G, Wang C and Fang J 2014 Solution-based synthesis of III–V quantum dots and their applications in gas sensing and bio-imaging *Nano Today* 9 69–84
- [29] Xie Y, Qian Y, Wang W, Zhang S and Zhang Y 1996 A benzene-thermal synthetic route to nanocrystalline GaN Science 272 1926–7
- [30] Mićić O I, Ahrenkiel S P, Bertram D and Nozik A J 1999 Synthesis, structure, and optical properties of colloidal GaN quantum dots Appl. Phys. Lett. 75 478–80
- [31] Manz A, Birkner A, Kolbe M and Fischer R A 2000 Solution synthesis of colloidal gallium nitride at unprecedented low temperatures Adv. Mater. 12 569–73
- [32] Grocholl L, Wang J and Gillan E G 2001 Solvothermal azide decomposition route to GaN nanoparticles, nanorods, and faceted crystallites *Chem. Mater.* 13 4290–6
- [33] Wang J, Grocholl L and Gillan E G 2002 Facile azidothermal metathesis route to gallium nitride nanoparticles *Nano Lett*. 2 899–902
- [34] Choi Y C, Kim H, Lee C, Son J, Baik H, Park S, Kim J and Jeong K S 2019 Blue emission of α -GaN colloidal quantum dots via Zn doping *Chem. Mater.* **31** 5370–5
- [35] Balkas C M, Basceri C and Davis R F 1995 Synthesis and characterization of high purity, single phase GaN powder Powder Diffr. 10 266–8
- [36] Purdy A P 1999 Ammonothermal synthesis of cubic gallium nitride Chem. Mater. 11 1648–51
- [37] Azuma Y, Shimada M and Okuyama K 2004 Synthesis of monodisperse ultrapure gallium nitride nanoparticles by MOCVD Chem. Vap. Depos. 10 11–3
- [38] Wang J C, Yu D P, Li C Y, Zhou J F, Wang Y Z and Feng S Q 2004 Large-scale synthesis of single-phase, high-quality GaN nanocrystallites Appl. Phys. A 78 753–5
- [39] Goodwin T J, Leppert V J, Risbud S H, Kennedy I M and Lee H W H 1997 Synthesis of gallium nitride quantum dots through reactive laser ablation Appl. Phys. Lett. 70 3122–4
- [40] Leppert V J, Zhang C J, Lee H W H, Kennedy I M and Risbud S H 1998 Observation of quantum confined excited states of GaN nanocrystals Appl. Phys. Lett. 72 3035–7
- [41] Yoon J-W, Sasaki T, Roh C H, Shim S H, Shim K B and Koshizaki N 2005 Quantum confinement effect of nanocrystalline GaN films prepared by pulsed-laser ablation under various Ar pressures *Thin Solid Films* 471 273–6
- [42] Li H D, Yang H B, Yu S, Zou G T, Li Y D, Liu S Y and Yang S R 1996 Synthesis of ultrafine gallium nitride powder by the direct current arc plasma method *Appl. Phys. Lett.* 69 1285–7

- [43] Shimada M, Wang W-N and Okuyama K 2010 Synthesis of gallium nitride nanoparticles by microwave plasmaenhanced CVD Chem. Vap. Depos. 16 151–6
- [44] Anthony R J, Thimsen E, Johnson J, Campbell S A and Kortshagen U 2005 Fast high-density low-pressure plasma synthesis of GaN nanocrystals MRS Online Proc. Libr. Arch. 892 FF11–05
- [45] You K H, Kim J H, You S J, Lee H C, Ruh H and Seong D J 2018 Gallium nitride nanoparticle synthesis using nonthermal plasma with gallium vapor *Curr. Appl. Phys.* 18 1553–7
- [46] Mangolini L, Thimsen E and Kortshagen U 2005 High-yield plasma synthesis of luminescent silicon nanocrystals *Nano Lett.* 5 655–9
- [47] Gresback R, Holman Z and Kortshagen U 2007 Nonthermal plasma synthesis of size-controlled, monodisperse, freestanding germanium nanocrystals *Appl. Phys. Lett.* 91 093119
- [48] Schramke K S, Qin Y, Held J T, Mkhoyan K A and Kortshagen U R 2018 Nonthermal plasma synthesis of titanium nitride nanocrystals with plasmon resonances at near-infrared wavelengths relevant to photothermal therapy ACS Appl. Nano Mater. 1 2869–76
- [49] Exarhos S, Alvarez-Barragan A, Aytan E, Balandin A A and Mangolini L 2018 Plasmonic core-shell zirconium nitride-silicon oxynitride nanoparticles ACS Energy Lett. 3 2349–56
- [50] Gresback R, Hue R, Gladfelter W L and Kortshagen U R 2011 Combined plasma gas-phase synthesis and colloidal processing of InP/ZnS core/shell nanocrystals *Nanoscale Res. Lett.* 6 68
- [51] Thimsen E, Kortshagen U R and Aydil E S 2015 Nonthermal plasma synthesis of metal sulfide nanocrystals from metalorganic vapor and elemental sulfur J. Phys. Appl. Phys. 48 314004
- [52] Felbier P, Yang J, Theis J, Liptak R W, Wagner A, Lorke A, Bacher G and Kortshagen U 2014 Highly luminescent ZnO quantum dots made in a nonthermal plasma Adv. Funct. Mater. 24 1988–93
- [53] Ann L P and Mohan S R 2011 Plasma-assisted dissociation of organometallic vapors for continuous, gas-phase preparation of multimetallic nanoparticles Angew. Chem., Int. Ed. Engl. 50 10953–6
- [54] Hoffman D M, Prakash Rangarajan S, Athavale S D, Economou D J, Liu J, Zheng Z and Chu W 1996 Chemical vapor deposition of aluminum and gallium nitride thin films from metalorganic precursors J. Vac. Sci. Technol. A 14 306–11
- [55] Koleske D D, Wickenden A E, Henry R L and Twigg M E 2002 Influence of MOVPE growth conditions on carbon and silicon concentrations in GaN J. Cryst. Growth 242 55–69
- [56] Deppert K, Bovin J-O, Malm J-O and Samuelson L 1996 A new method to fabricate size-selected compound semiconductor nanocrystals: aerotaxy *J. Cryst. Growth* 169 13–9
- [57] Deppert K and Samuelson L 1996 Self-limiting transformation of monodisperse Ga droplets into GaAs nanocrystals Appl. Phys. Lett. 68 1409–11
- [58] Heurlin M, Magnusson M H, Lindgren D, Ek M, Wallenberg L R, Deppert K and Samuelson L 2012 Continuous gas-phase synthesis of nanowires with tunable properties *Nature* 492 90–4
- [59] Kortshagen U R, Sankaran R M, Pereira R N, Girshick S L, Wu J J and Aydil E S 2016 Nonthermal plasma synthesis

- of nanocrystals: fundamental principles, materials, and applications *Chem. Rev.* **116** 11061–127
- [60] Uner N B and Thimsen E 2017 In-flight size focusing of aerosols by a low temperature plasma J. Phys. Chem. C 121 12936–44
- [61] Alcock C B, Itkin V P and Horrigan M K 1984 Vapour pressure equations for the metallic elements: 298–2500 K Can. Metall. Q. 23 309–13
- [62] Uner N B and Thimsen E 2018 Low temperature plasma as a means to transform nanoparticle atomic structure *Plasma* Sources Sci. Technol. 27 074005
- [63] Holman Z C and Kortshagen U R 2010 A flexible method for depositing dense nanocrystal thin films: impaction of germanium nanocrystals *Nanotechnology* 21 335302
- [64] Li C, Singh N, Andrews A, Olson B A, Schwartzentruber T E and Hogan C J 2019 Mass, momentum, and energy transfer in supersonic aerosol deposition processes *Int. J. Heat Mass Transf.* 129 1161–71
- [65] Kennedy J L and Djeu N 2002 Operation of Yb:YAG fiberoptic temperature sensor up to 1600 °C Sensors Actuators A 100 187–91
- [66] Kennedy J L and Djeu N 2003 Energy transfer in rare earth doped Y₃Al₅O₁₂ at very high temperatures *J. Lumin*. 101 147–53
- [67] Neild S T, Skowronski M and Lagowski J 1991 Signature of the gallium–oxygen–gallium defect in GaAs by deep level transient spectroscopy measurements Appl. Phys. Lett. 58 859–61
- [68] Tansley T L, Egan R J and Horrigan E C 1988 Properties of sputtered nitride semiconductors *Thin Solid Films* 164 441–8
- [69] Bao K, Guo G, Zhang L, Liu R, Sun H and Zhong Z 2011 Controlled synthesis of GaN@SiO₂ particles in preventing the hydrolysis of GaN J. Phys. Chem. C 115 13200–6
- [70] Kolesova V A and Ryskin Ya I 1962 Infrared absorption spectra of diaspore (α-AlOOH). Boehmite (γ-AlOOH) and GaOOH J. Struct. Chem. 3 656–9
- [71] Lai Y-H, Yeh C-T, Hwang J-M, Hwang H-L, Chen C-T and Hung W-H 2001 Sputtering and etching of GaN Surfaces J. Phys. Chem. B 105 10029–36
- [72] Kovač J and Zalar A 2002 Surface composition changes in GaN induced by argon ion bombardment Surf. Interface Anal. 34 253–6
- [73] Yamane H, Shimada M, Clarke S J and DiSalvo F J 1997 Preparation of GaN single crystals using a Na flux *Chem. Mater.* 9 413–6
- [74] Wang B, Callahan M J, Rakes K D, Bouthillette L O, Wang S-Q, Bliss D F and Kolis J W 2006 Ammonothermal growth of GaN crystals in alkaline solutions J. Cryst. Growth 287 376–80
- [75] Daugherty J E and Graves D B 1993 Particulate temperature in radio frequency glow discharges J. Vac. Sci. Technol. A 11 1126–31
- [76] Mangolini L and Kortshagen U 2009 Selective nanoparticle heating: another form of nonequilibrium in dusty plasmas *Phys. Rev.* E 79 026405
- [77] Maurer H R and Kersten H 2011 On the heating of nano- and microparticles in process plasmas J. Phys. Appl. Phys. 44 174029
- [78] Kramida A, Ralchenko Y, Reader J and NIST ASD Team 2019 NIST Atomic Spectra Database version 5.7.1 (https://physics.nist.gov/asd) (Accessed: 1 December 2019) (Gaithersburg, MD: National Institute of Standards and Technology) (https://doi.org/10.18434/T4W30F)

- [79] Qin Y, Bilik N, Kortshagen U R and Aydil E S 2016 Laser light scattering from silicon particles generated in an argon diluted silane plasma J. Phys. Appl. Phys. 49 085203
- [80] Emeleus K G and Breslin A C 1970 Notes on the effects of dust in positive columns Int. J. Electron. 29 1–18
- [81] Von Engel A 1994 Ionized Gases (AIP Press: Woodbury, NY)
- [82] Clements R M 1978 Plasma diagnostics with electric probes *J. Vac. Sci. Technol.* **15** 193–8
- [83] Coleman D, Lopez T, Yasar-Inceoglu O and Mangolini L 2015 Hollow silicon carbide nanoparticles from a non-thermal plasma process J. Appl. Phys. 117 193301
- [84] Wheeler L M, Kramer N J and Kortshagen U R 2018 Thermodynamic driving force in the spontaneous formation of inorganic nanoparticle solutions *Nano Lett.* 18 1888–95

- [85] Reshchikov M A and Morkoç H 2005 Luminescence properties of defects in GaN J. Appl. Phys. 97 061301
- [86] Chen T, Reich K V, Kramer N J, Fu H, Kortshagen U R and Shklovskii B I 2016 Metal-insulator transition in films of doped semiconductor nanocrystals *Nat. Mater.* 15 299–303
- [87] Lanigan D and Thimsen E 2016 Contact radius and the insulator–metal transition in films comprised of touching semiconductor nanocrystals ACS Nano 10 6744–52
- [88] Thimsen E, Johnson M, Zhang X, Wagner A J, Mkhoyan K A, Kortshagen U R and Aydil E S 2014 High electron mobility in thin films formed via supersonic impact deposition of nanocrystals synthesized in nonthermal plasmas *Nat. Commun.* 5 5822

SUPPORTING INFORMATION FOR:

Nonequilibrium plasma aerotaxy of size controlled GaN nanocrystals

Necip B. Uner¹ and Elijah Thimsen^{1,2}

Experimental Setup - Photos and Figures.

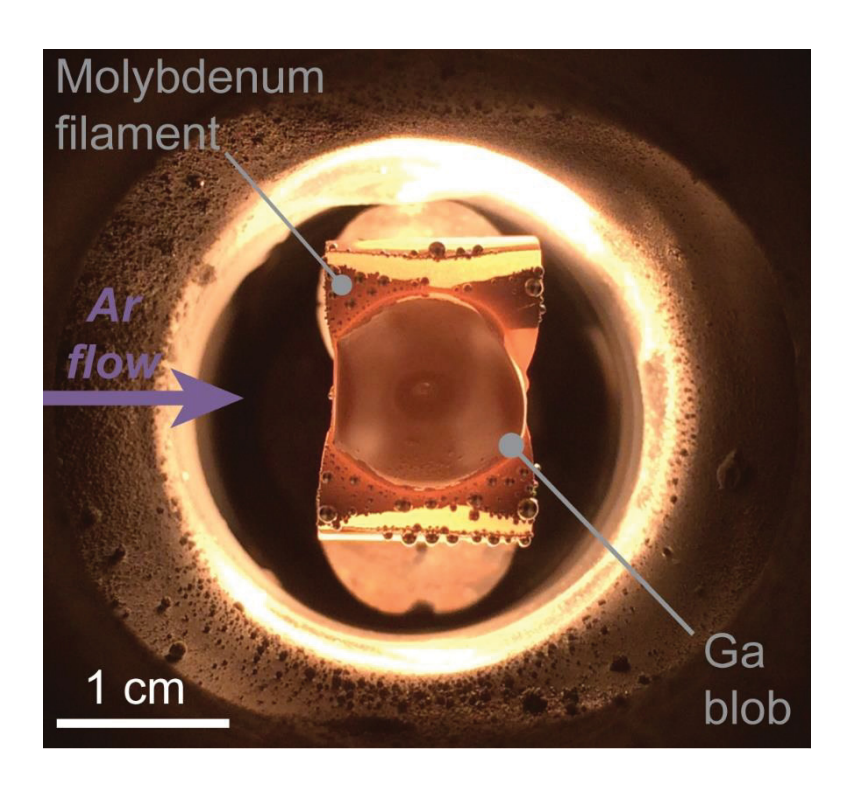


Figure S1. Hot Filament Evaporator. Liquid Ga on an alumina-coated Mo filament.

¹Department of Energy, Environmental and Chemical Engineering, Washington University in St. Louis, 1 Brookings Dr, St. Louis, MO 63130, USA.

²Institute for Materials Science and Engineering, Washington University in St. Louis, 1 Brookings Dr., St. Louis, MO 63130, USA

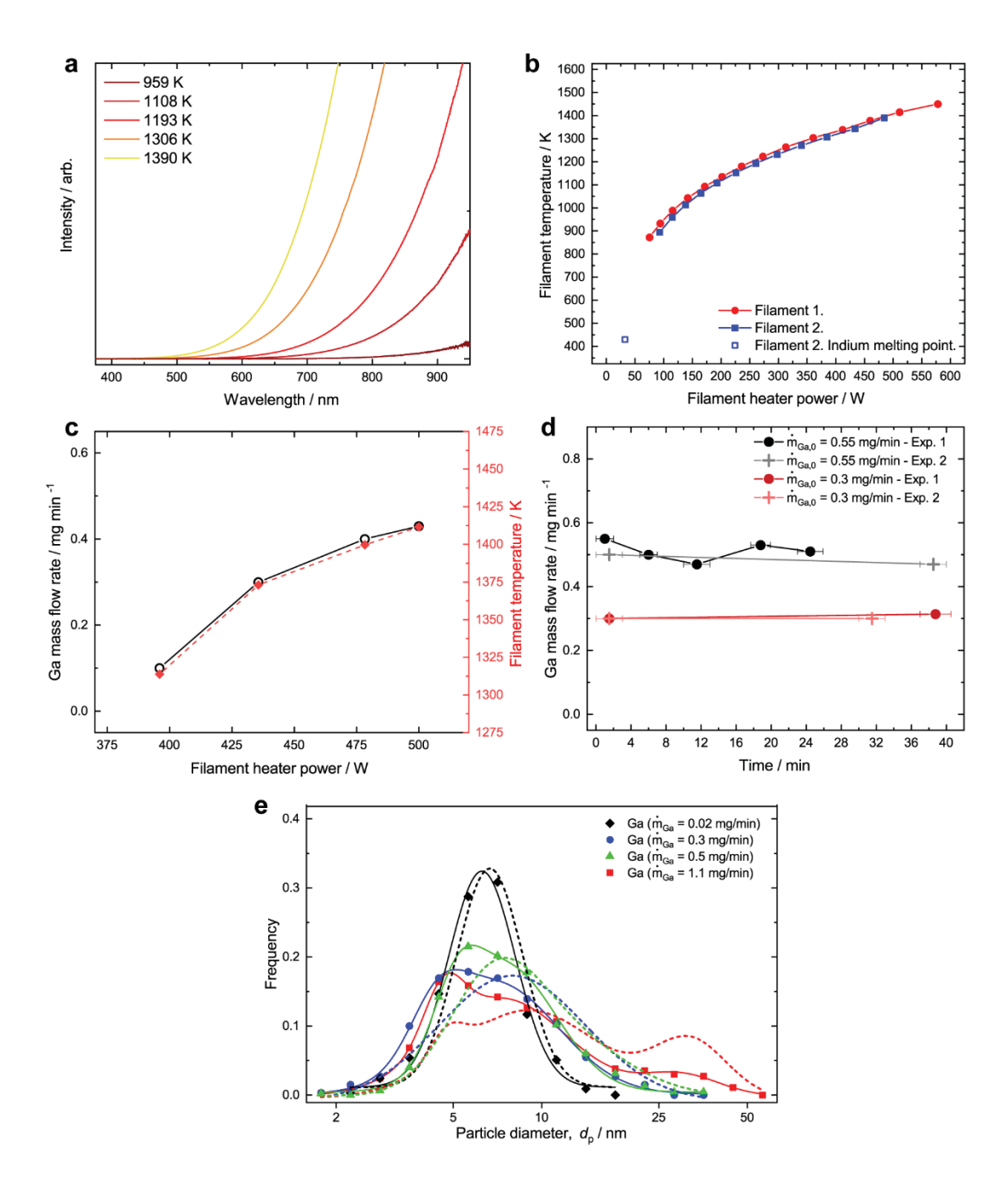


Figure S2. Characterization of the hot-filament evaporator. (a) Blackbody radiation emitted by the Ga blob. Curves were acquired at different powers applied to the filament. (b) Filament temperature as a function of applied power. Measurements were done for two different filaments at 4.2 Torr with 500 sccm Ar flow. (c) Evaporator output and filament temperature as function of applied power. (d) Evaporator output as a function of time. (e) Frequency distributions of the Ga aerosols produced. Dotted curves are the distributions corrected for collection efficiency (*vide infra*). Mass flow rates given in panels (c-e) are the values measured on filters, and due to filter collection efficiency being approximately 50%, actual flow rates were 2 times higher.

Additional size distributions: Effect of aerosol mass flow rate.

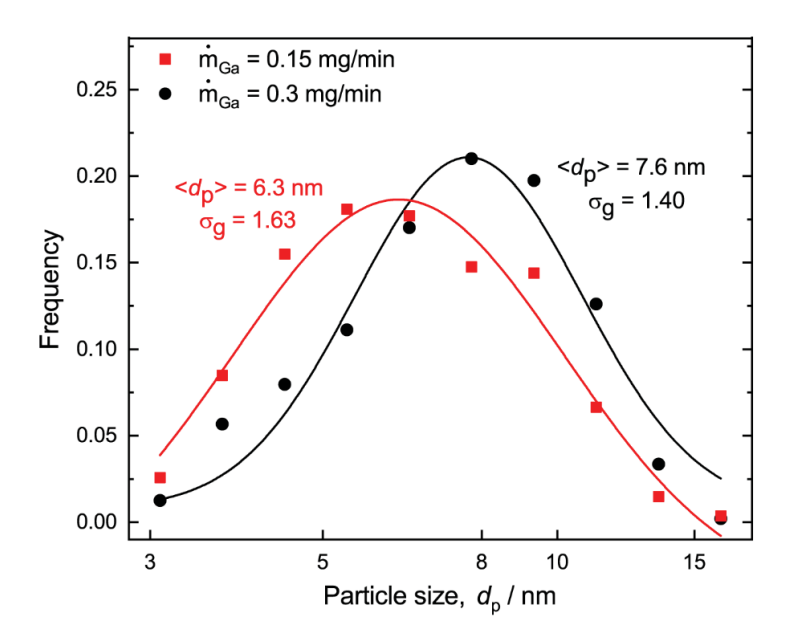


Figure S3. Effect of aerosol mass input on mean particle size. The following operation conditions were employed: Pw = 80 W, P = 4.2 Torr, $\tau = 17 \text{ ms}$, $Ar: N_2 = 25$.

Additional Data on Hollow Particles

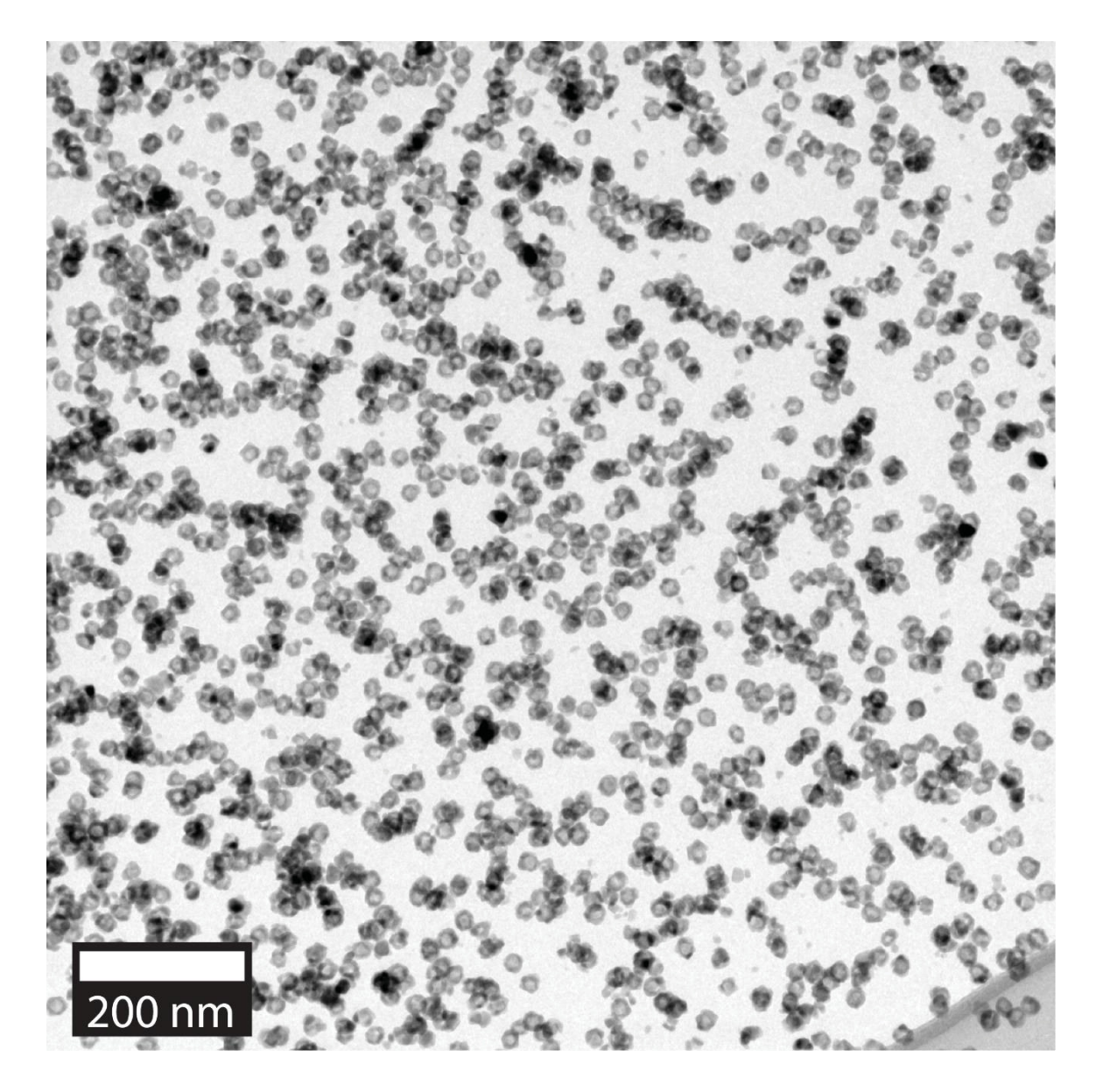


Figure S4. Overview of monodisperse hollow GaN particles. Particles were synthesized at the following conditions: Pw = 80 W, P = 6 Torr, $\tau = 64 \text{ ms}$, $Ar: N_2 = 25$, $\dot{\mathbf{m}}_{Ga} = 0.3 \text{ mg/min}$. $< d_p > = 23 \text{ nm}$ and $\sigma_g = 1.12$.

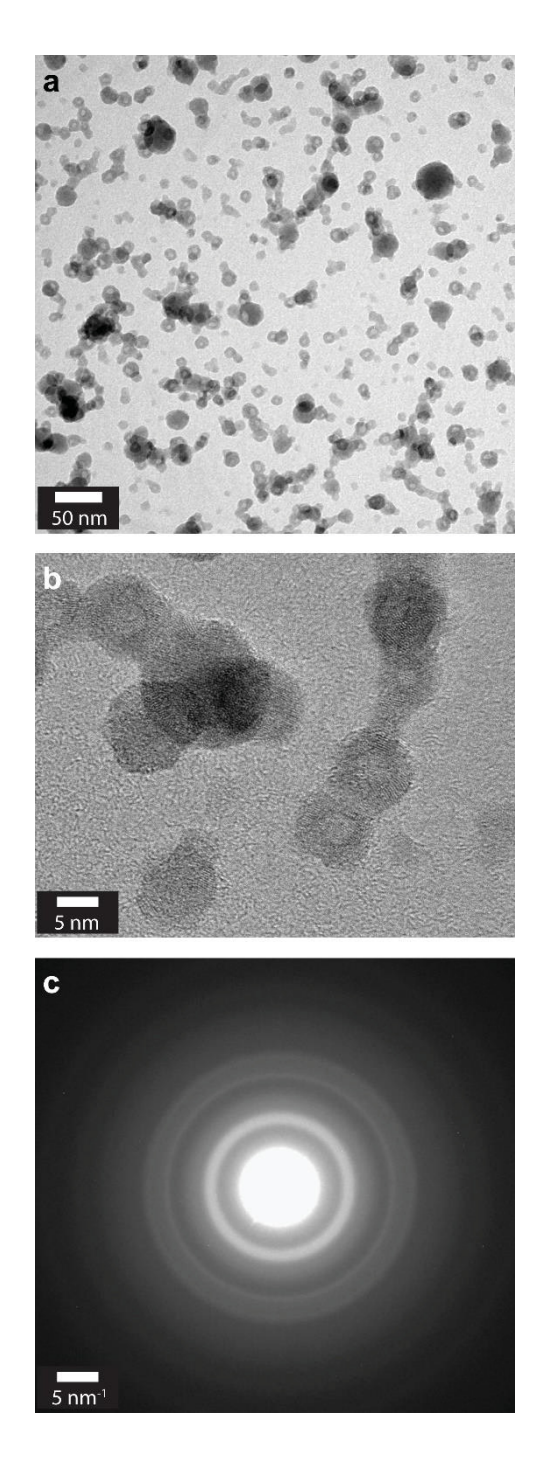


Figure S5. Hollow particles obtained at low power (20W). (a) Low magnification TEM image of small and hollow particles, together with large and solid particles. Large particles are unreacted Ga. (b) HRTEM image of hollow particles. (c) SAED pattern. The hazy rings indicate either very small crystallites (e.g. on the shell of hollow particles) or partially amorphous Ga particles. Following conditions were used: Pw = 20 W, P = 4.2 Torr, $\tau = 17 \text{ ms}$, $Ar: N_2 = 25$, $\dot{\mathbf{m}}_{Ga} = 0.3 \text{ mg/min}$.

SAED Analysis.

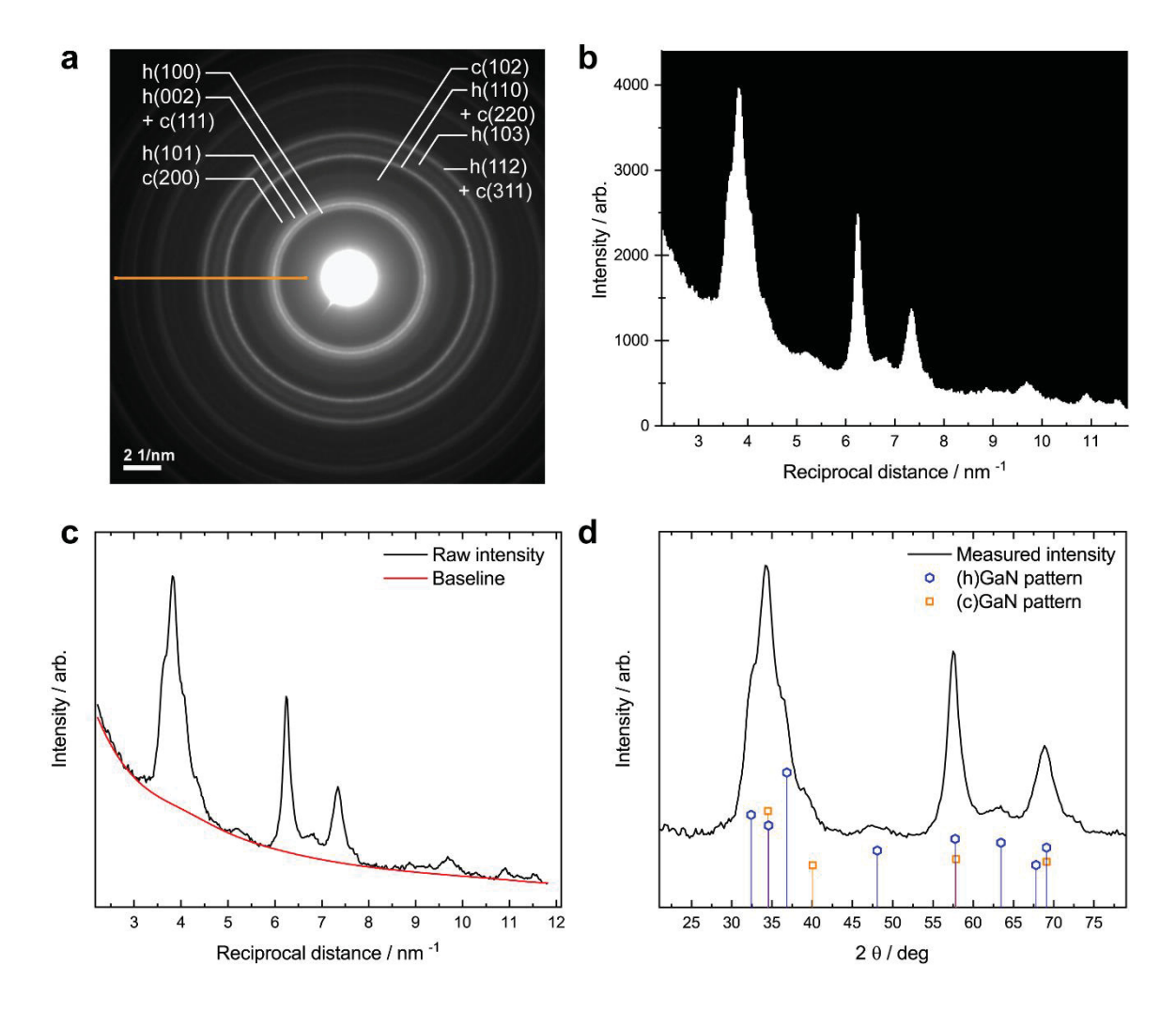


Figure S6. Sample selective area electron diffraction in TEM. (a) A SAED pattern obtained on GaN NCs. Debye-Scherrer rings belonging to both the cubic and hexagonal phases were visible. Intensity data was acquired on the orange line. (b) Raw intensity data. The resolution was limited by the camera. (c) Intensity data and baseline correction to remove the bleed-off of light from the central bright spot. (d) Baseline-subtracted data plotted analogous to data obtained from a Cu K α x-ray source. The electron diffraction patterns were almost equivalent with the XRD patterns given in Figure 3 in the main text, indicating that preferential orientation in XRD measurements is absent, and the particles are roughly spherical.

Rietveld Refinement and Quantitative Analysis.

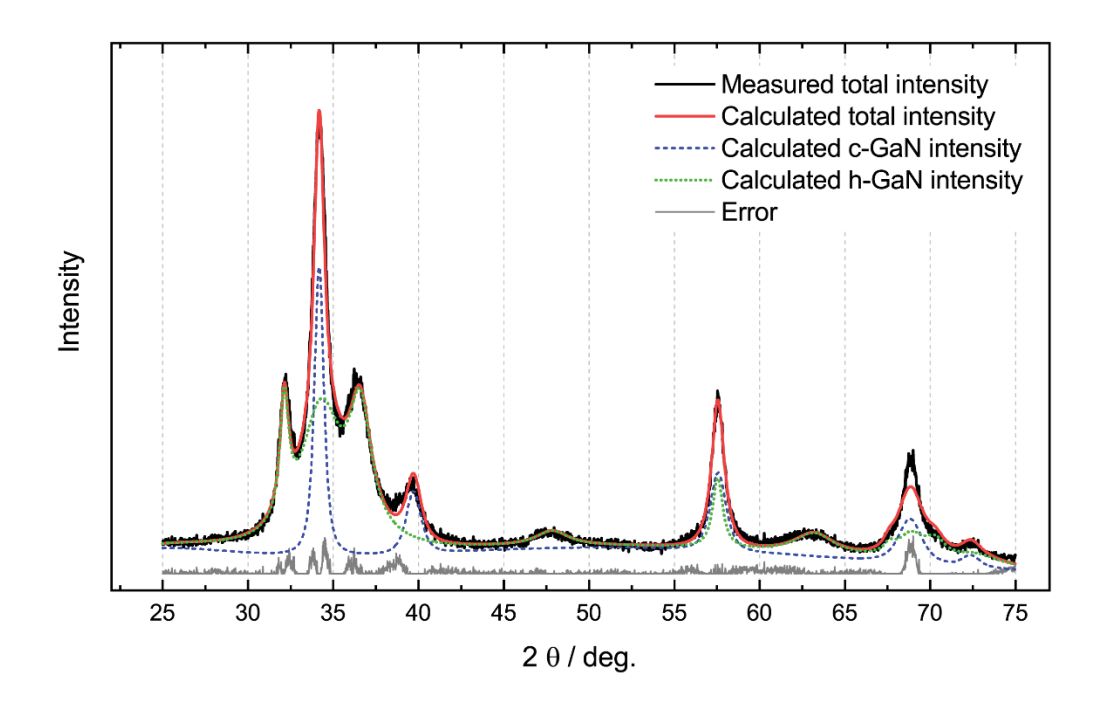


Figure S7. Sample Rietveld refinement. Fitting was done by using Profex software[1]. The presence of only a few, wide and asymmetric peaks made fitting somewhat difficult (Rietveld error parameters: $R_{wp} = 8.93$ %, $R_{exp} = 5.2$ %, $\chi^2 = 2.95$). The phase ratio of this sample was found to be 67% hexagonal, 33% cubic (2:1). The sample had a mean size of 10.2 nm (TEM) and had crystallite sizes of 9 and 11 nm as determined with the Scherrer equation from the first peaks of the hexagonal and cubic phase respectively.

ATR-FTIR Spectroscopy

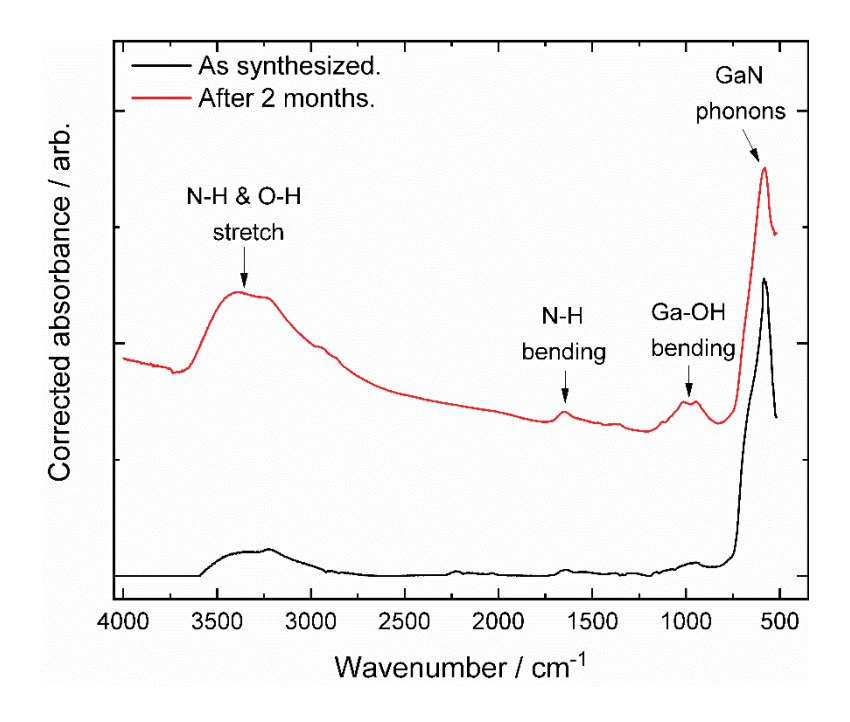


Figure S8. Evolution of FTIR spectra with time. The spectrum corresponding to as synthesized GaN powder and the spectrum corresponding to the same sample stored under ambient conditions for 2 months are given.

Determination of GaN Stoichiometry.

Energy Dispersive X-Ray Spectroscopy (EDXS):

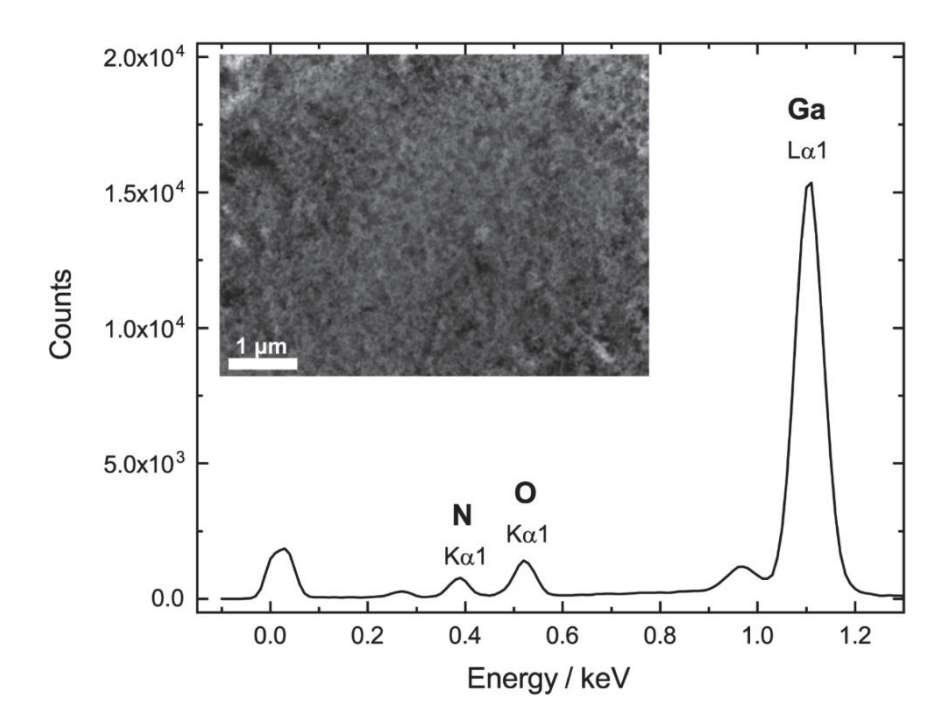


Figure S9. EDXS in SEM on GaN powder. A sample EDXS spectrum is given. The inset shows the flattened surface of fine and uniform GaN powder used for acquiring the spectrum.

Thermogravimetric Analysis (TGA):

TGA was used to estimate the Ga:N ratio in the NCs. The following general reaction describes the oxidation of Ga-rich GaN at elevated temperatures under air atmosphere:

$$(\gamma-1) Ga_{(s)} + GaN_{(s)} + (3\gamma/2) O_{2(g)} \rightarrow (\gamma/2) Ga_2O_3 + \frac{1}{2} N_{2(g)}$$

This reaction neglects the presence of any surface oxide before oxidation. Formation of any sub-oxide during TGA is omitted. Under these assumptions, one can write the following equation for the Ga:N ratio, which is represented by γ , as a function of relative change in the mass of the powder, $\Delta m/m_0$, where Δm is the difference between the final and initial powder mass (m_0) .

$$\gamma = \frac{MW_{GaN} - MW_{Ga}}{\frac{1}{1 + \Delta m/m_0} \frac{MW_{Ga_2O_3}}{2} - MW_{Ga}}$$
 (S1)

MW stands for molecular weight. An equivalent expression is obtained when one assumes that GaN is initially nitrogen-rich. During TGA, powders were heated up to 1123 K.

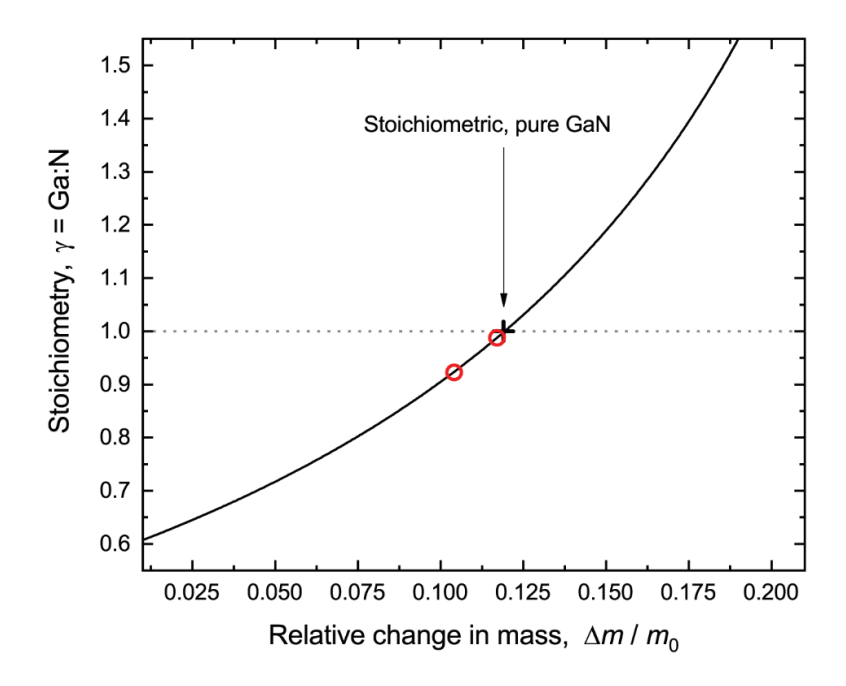


Figure S10. TGA analysis of GaN stoichiometry. Black line represents Equation (S1). The cross indicates GaN with exactly 1:1 stoichiometry. Red circles are measurements made on different powders.

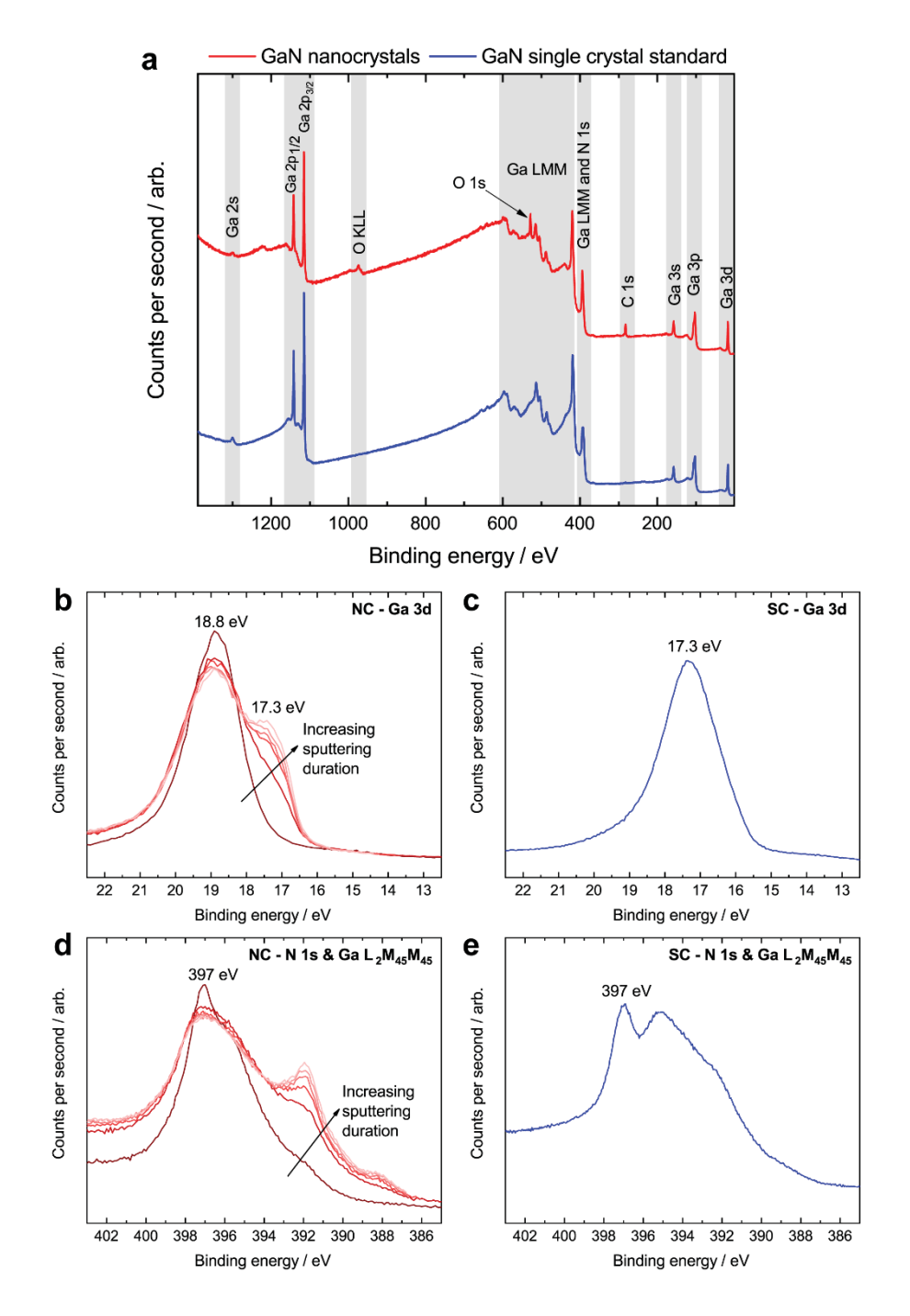


Figure S11. XPS results on GaN NCs and GaN reference single crystal (SC). (a) Survey spectra. (b,c) Ga 3d peaks of the NCs and the SC respectively. Sputtering durations were incrementally increased by 1 minute. (d,e) N 1s and Ga Auger peaks of the NCs and the SC. Sputtering durations were similar to as in (b,c).

Color of NC dispersions:

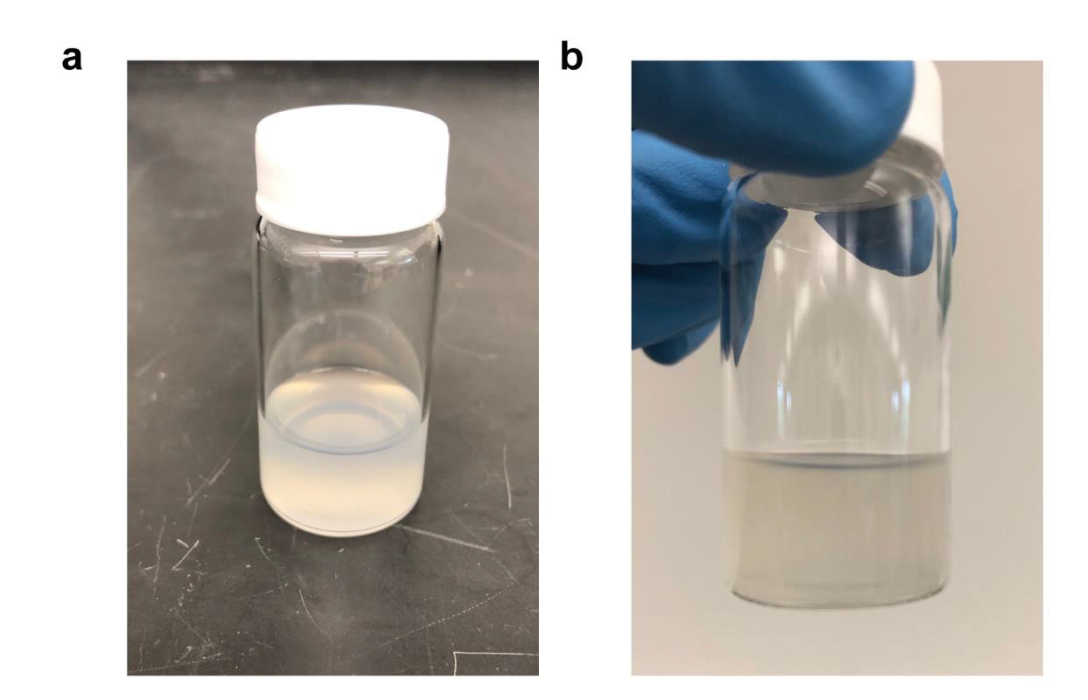


Figure S12. Dispersion of bare GaN NCs in methanol. Against (a) black and (b) white background.

Computational fluid dynamics (CFD) and the calculation of collection efficiency on TEM grids.

During the preparation of TEM samples, a TEM grid was vertically suspended downstream of the plasma. To suspend the grid, it was attached onto an adhesive tape which was then attached to a stainless steel mesh filter. The grid lies at the center of the tubular flow path. As particles flow onto the grid, some of them end up getting deposited due to the three major mechanisms of aerosol collection in play: diffusion, interception and impaction. Finite-element based CFD (COMSOL 5.3) was used to simulate fluid flow and particle deposition on the grid to obtain the particle capture efficiency as a function of particle diameter. Results can be used to relate the particles collected on the grid with the aerosol synthesized by the plasma.

Figure S13 shows the calculation domain, which is drawn in axisymmetric geometry. The thickness of the grid and tape assembly was approximately 1 mm. Due to relatively low experimental pressure drop measured across the filter, the filter was omitted in the simulations.

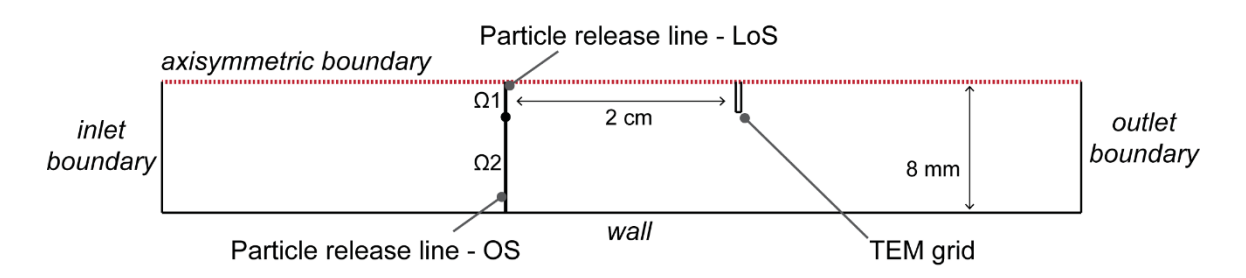


Figure S13. Computational domain employed in CFD calculations. Total length of the domain was 14 cm.

Since the flow field and particle deposition are decoupled, first, the flow field was resolved. Incompressible Navier-Stokes equations were solved with second and first order elements for velocity and pressure respectively. An adaptive mesh was used to obtain an accurate flow field nearby the grid (Figure S14). All flow calculations were done at 293 K with Ar only.

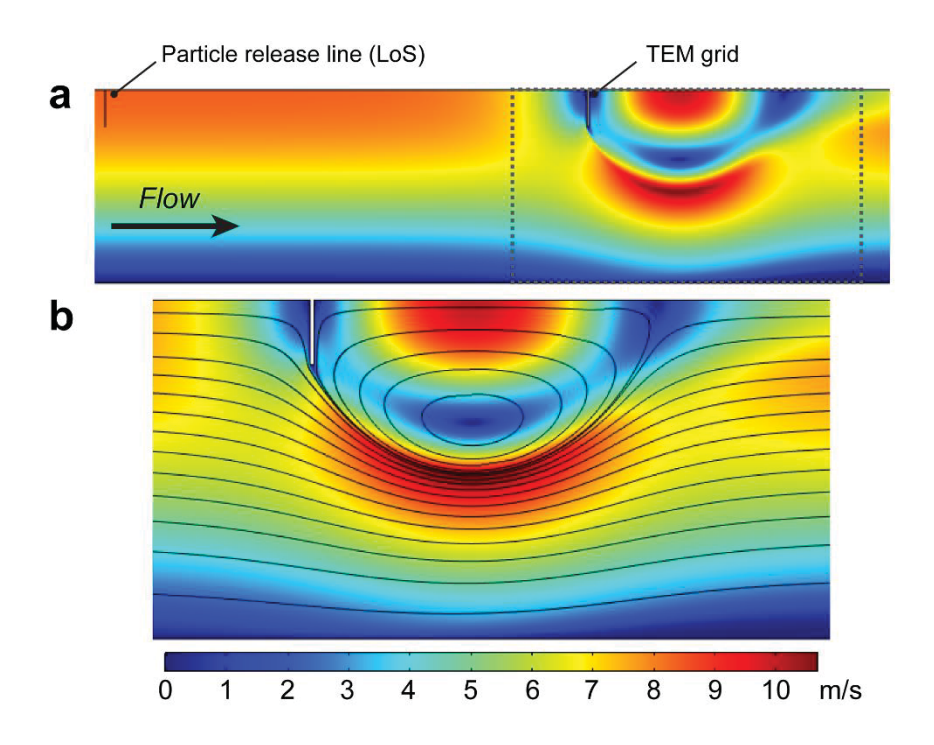


Figure S14. Flow field. (a) View of the flow field at 4.2 Torr and with 4.2 m/s mean inlet velocity (260 sccm total flow). The range of velocities are defined by the color bar given below. (b) Zoomed-in view of the boxed region in (a). Streamlines indicated the formation of a vortex downstream of the grid at all conditions investigated.

Once the flow field is in hand for a given pressure and average inlet velocity, the field can be used for particle tracking to simulate TEM sampling. The Langevin equation[2] was solved for a minimum of 1200 particles. Using slip-corrected Stokes drag[3] allowed direct modelling of interception and impaction. incorporated into the Langevin equation as white noise[4] (Figure S15). Particles were released from a radial line that is placed at a distance of 2 cm from the grid (Ω_1 in Figure S13). This distance was selected carefully. At this distance, there was little to no diffusion loss to the walls other than the grid, and the flow field was unaffected by the grid. The release line had the radius of the TEM grid (1.525 mm, Ω_1 in Figure S13). This particle input is called as the line-of-sight (LoS) release. Due to the increased diffusion lengths at low pressure, some particles at positions radially further away from the end of Ω_1 was found to be able to diffuse on to the grid. This effect was capable of increasing the collection efficiency of particles that are smaller than 15 nm. Therefore, for such small sizes, particles were released from the outer annular shell as well (abbreviated as OS, Ω_2 in Figure S13). The relative number of particles released from this shell was adjusted by assuming that the particle number concentration had a near parabolic profile across the radial dimension. We defined the collection efficiency as:

$$\eta = \frac{N_{deposited}^{LoS} + N_{deposited}^{OS}}{N_{released}^{LoS}}$$
 (S2)

where N stands for the number of particles. The collection efficiency, calculated by Equation S2, is a relative property. Therefore, it doesn't exactly provide how many particles deposit on the grid across the whole radial dimension, but it determines the relative capture efficiency of particles of different sizes. Therefore, the value of this relative η can be larger than 1 for very small clusters.

Particle size range between 5-5000 nm was scanned and the capture efficiency plots were generated by using equation (S2) (Figure S16). Particles smaller than 5 nm were not explored due to very long CPU times required. The capture efficiency can be used to invert the size distributions obtained from TEM analysis, and consequently the size distribution of the flowing aerosol can be calculated (Figure S17).

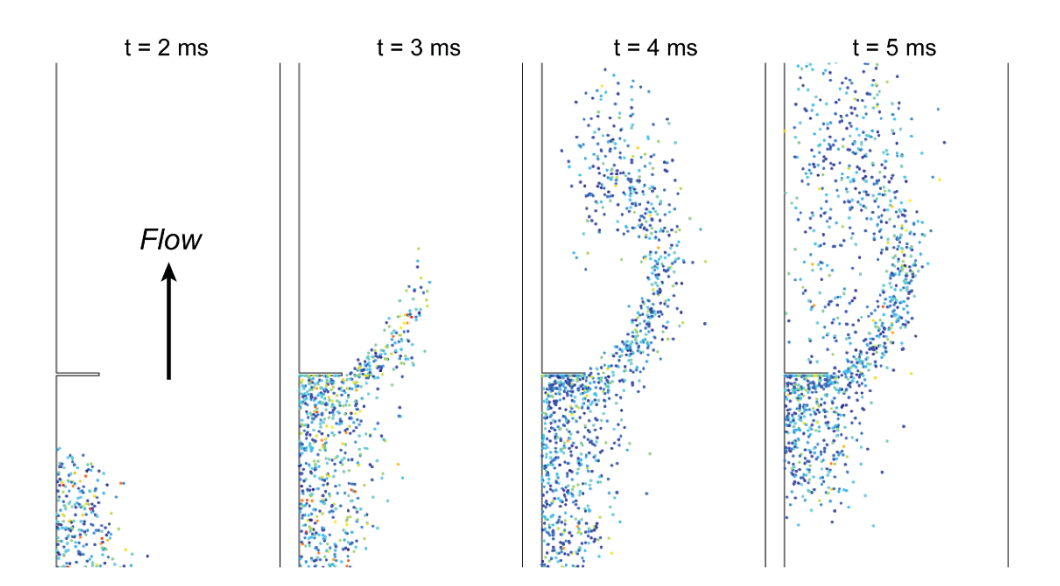


Figure S15. Deposition of 10 nm particles on the TEM grid as a function of time. Frames demonstrate the particle collection simulations during LoS release. Particle sizes in the frames above were greatly exaggerated for better visibility. Different colors represent different particle velocities. Diffusion lead to significant gradients in particle concentrations. Simulation was run at 4.2 Torr pressure and with 4.2 m/s inlet velocity.

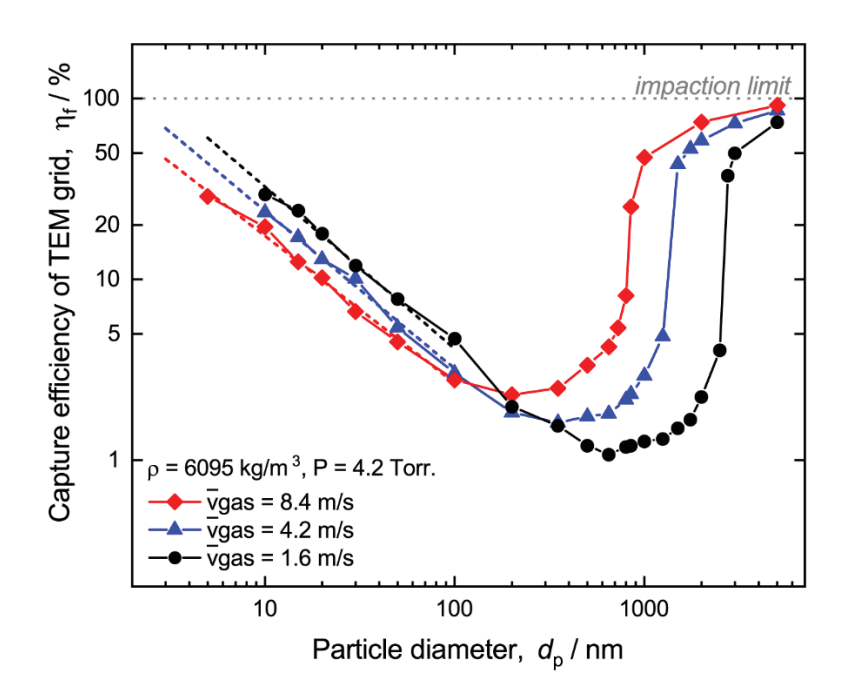


Figure S16. Particle capture efficiency on TEM grids. The dashed lines are the fits used for the GaN NCs synthesized in this study. Their main mechanism of deposition is diffusion.

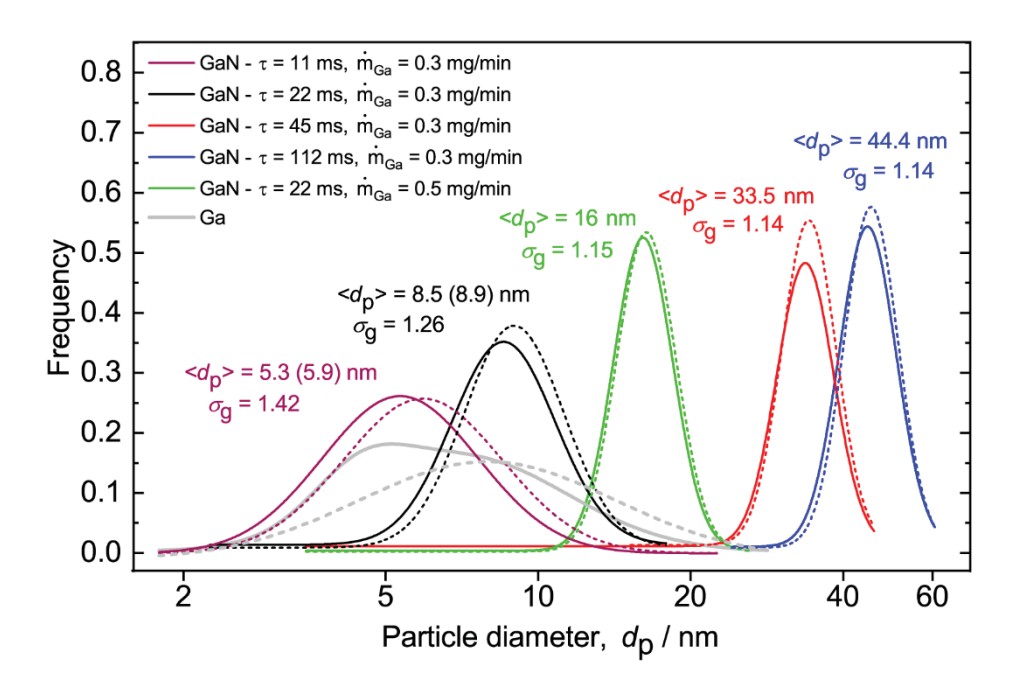


Figure S17. Inversion of the particle size distributions obtained from TEM. Solid lines are lognormal fits to the distributions obtained from TEM images. The dashed lines are the lognormal fits to the inverted data. Mean particle sizes change slightly for the widest distributions (corrected values are given in parentheses). Greatest shift was observed for the Ga aerosol. Geometric standard deviations were mostly unchanged after inversion.

Plasma Characterization.

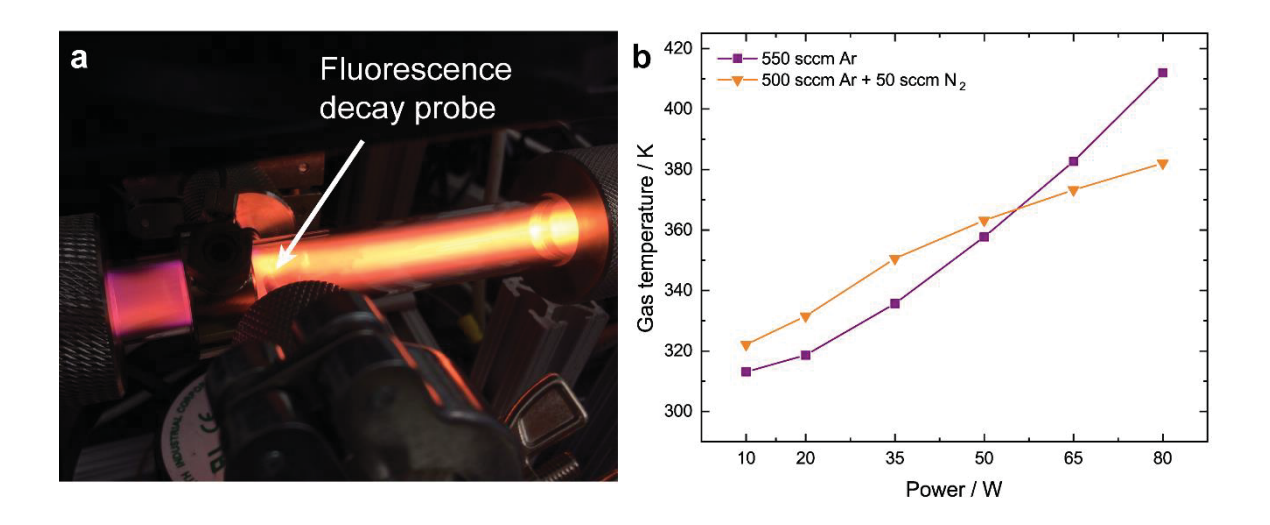


Fig. S18. Background gas temperature in the plasma. (a) A cross-shaped glass tube were used to insert the fluorescence decay probe just downstream of the powered electrode. (b) Measured gas temperature values as a function of power. Pressure was 6 Torr. Fans were kept on during the measurements.

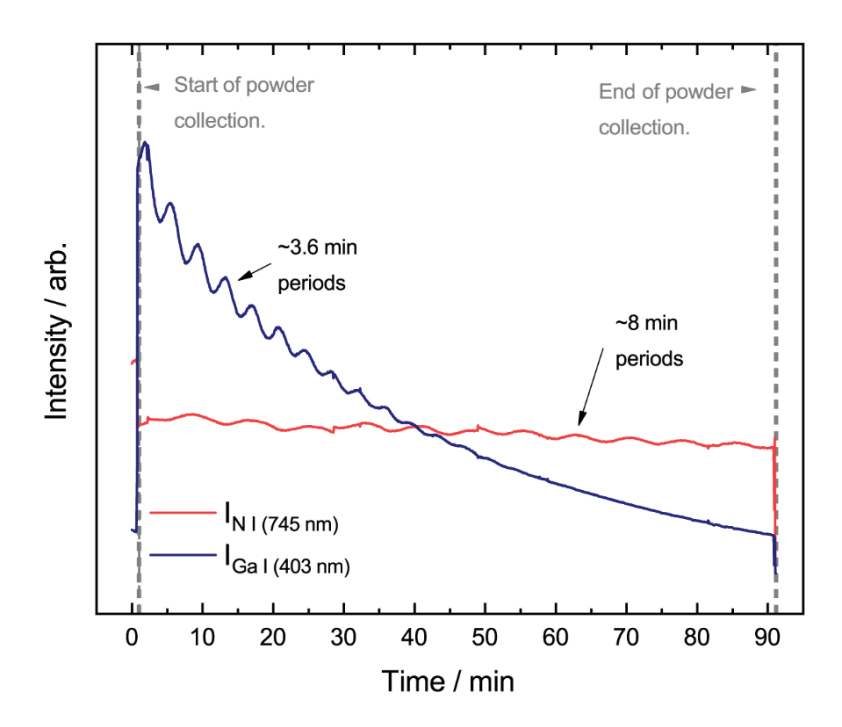


Fig. S19. Fluctuations in emission lines. The data was collected during powder collection downstream of the powered electrode (4 cm position in Figure 8 in the main text). The decrease in the intensity of Ga I emission is due to the formation of a yellowish film on the tube walls. The film, likely a form of nonstoichiometric GaN, absorbs the Ga I emission but it is mostly transparent to the N I emission. The fluctuations were observed in all experiments, although their periods differed slightly.

Double Langmuir probe I-V Curve Analysis

I-V curves recorded by the double Langmuir probe were analyzed to obtain the electron temperature and ion density. The classical method outlined by Raizer[5], which assumes Maxwellian electrons, were employed to extract electron temperature. Ion densities were obtained from the following expression:

$$n_i = J_i^{sat} \left(\frac{1 + 5\lambda_{De}/\lambda_i}{0.52\nu_B} \right) \tag{S3}$$

In Equation S3, $J_i^{\rm sat}$ is the saturation current density, which is saturation current divided by the probe area. v_B is Bohm velocity, and the nominator in the parentheses is an empirical factor that accounts for ion-neutral collisions[6]. $\lambda_{\rm De}$ is the electron Debye length, $\lambda_{\rm De} = (\varepsilon_0 k_{\rm B} T_{\rm e}/e^2 n_{\rm i})^{1/2}$, where ε_0 is the permittivity of vacuum, $k_{\rm B}$ is the Boltzmann constant, $T_{\rm e}$ is the electron temperature, e is the unit charge and $n_{\rm i}$ is the ion density. $\lambda_{\rm i}$ is the ion mean free path, $\lambda_{\rm i} = k_{\rm B} T_{\rm i}/V2\sigma_{\rm i}P$. $T_{\rm i}$ is the ion temperature, P is pressure and $\sigma_{\rm i}$ is the ion-neutral cross-section[7]. The accuracy of Equation S3 is similar to the accuracy of the modified Talbot-Chou model[8]. In analysis, it was assumed $T_{\rm i} = T_{\rm gas}$, where $T_{\rm gas} = 380$ K. Furthermore, all ions are assumed to be Ar⁺, based on calculations indicating that the concentration of N_2^+ ions in similar Ar/ N_2 plasmas is two orders of magnitude lower than that of Ar⁺ ions[9]. During measurements, the tips were exposed to the plasma for only a few seconds to minimize contamination.

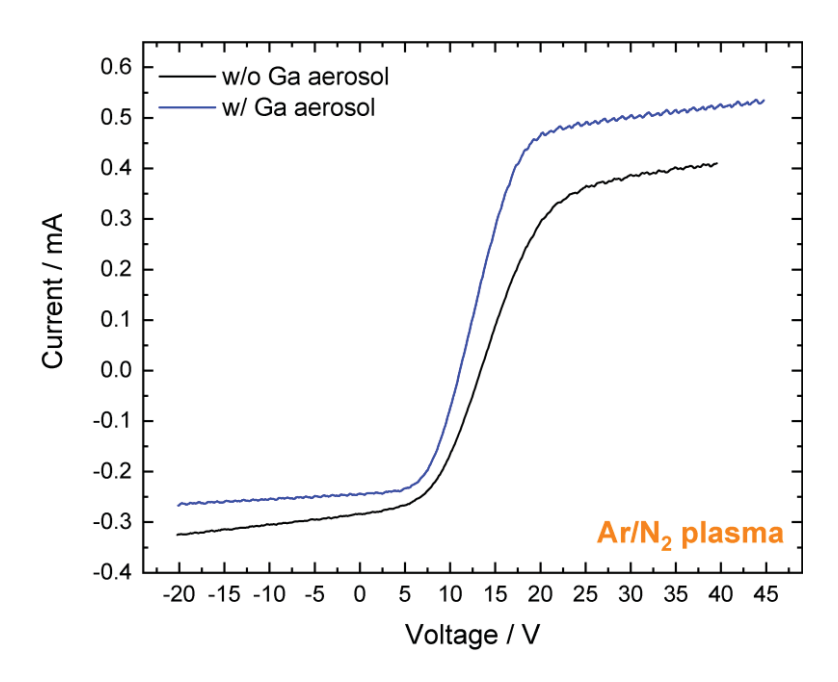


Fig. S20. Sample I-V curves. The following conditions were used: P = 4.2 Torr and Ar:N₂ = 25. Tube ID was 16 mm.

Table. S1. Summary of double Langmuir probe measurements made in the Ar/N₂ plasma. Values reported are the averages of at least three measurements. The increase in ion density after cleaning the tips with fine sandpaper can be attributed to the increased roughness of the surface of the tips.

	$k_{\rm B}T_{\rm e}$ (eV)	n _i x 10 ¹⁸ (m ⁻³)
Fresh tips, no aerosol	2.74 ± 0.07	1.78 ± 0.02
w/ Ga aerosol	2.30 ± 0.02	2.05 ± 0.12
Coated tips, no aerosol	2.01 ± 0.03	1.79 ± 0.01
Tips cleaned with fine sandpaper	2.69 ± 0.06	2.28 ± 0.01

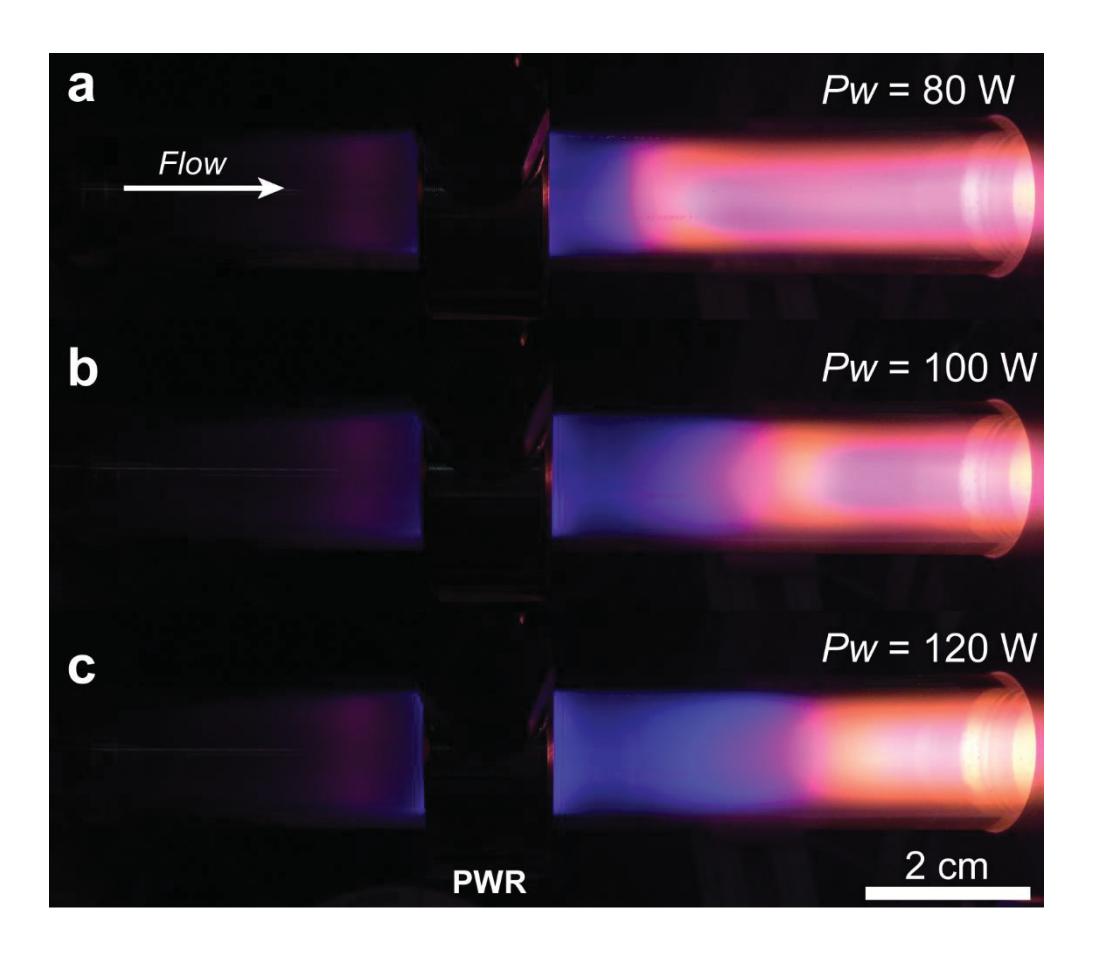


Fig. S21. Expansion of the blue vaporization zone with increasing power. Photos were taken when the following parameters were used: P = 4.2 Torr, $\tau = 22 \text{ ms}$, $\text{Ar:N}_2 = 25$, $\dot{m}_{\text{Ga}} = 0.5 \text{ mg/min}$. A similar expansion of the vaporization zone was observed when pressure was decreased from 4.2 Torr to 2 Torr (not shown).

Stability of NC dispersions

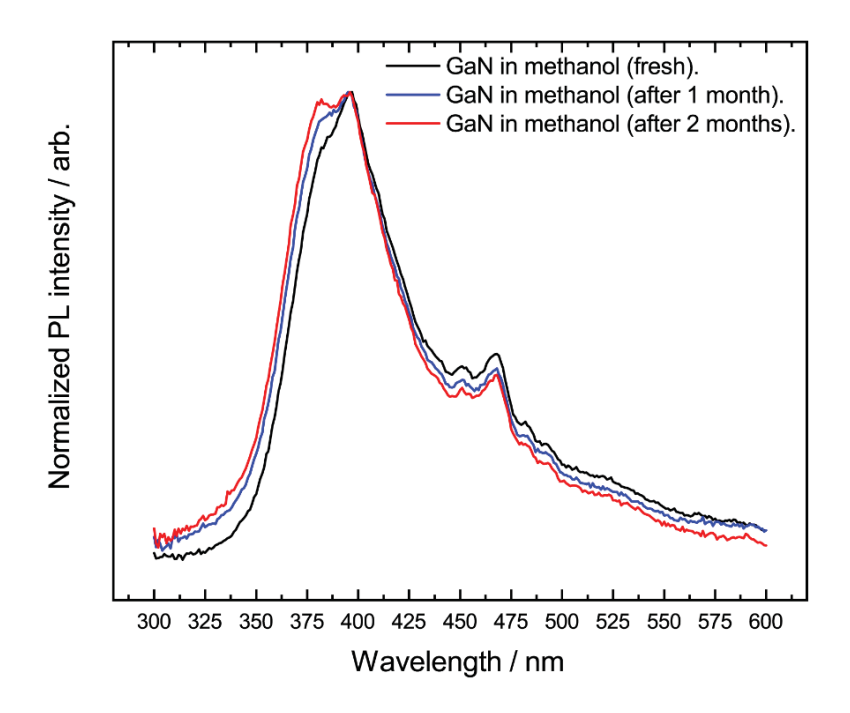


Fig. S22. Stability of band gap emission. GaN NCs were dispersed in methanol.

GaN NC film

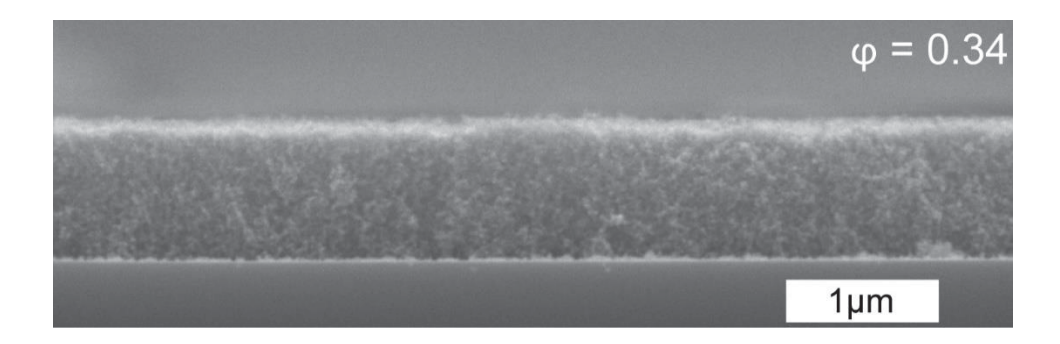


Fig. S23. SEM image of a film comprised of GaN NCs. The film was porous, with 34% fill fraction (ϕ) and 900 nm thickness. Mean particle size was approximately 35 nm.

References

- [1] Doebelin N and Kleeberg R 2015 Profex: a graphical user interface for the Rietveld refinement program BGMN *J. Appl. Crystallogr.* **48** 1573–80
- [2] Ermak D L and Buckholz H 1980 Numerical integration of the Langevin equation: Monte Carlo simulation *J. Comput. Phys.* **35** 169–82
- [3] Friedlander S K 2000 *Smoke, dust, and haze: fundamentals of aerosol dynamics* (New York: Oxford University Press)
- [4] Chandrasekhar S 1943 Stochastic Problems in Physics and Astronomy *Rev. Mod. Phys.* **15** 1–89
- [5] Raizer Y 1997 Gas discharge physics (Berlin; New York: Springer)
- [6] Iza F and Lee J K 2006 Particle-in-cell simulations of planar and cylindrical Langmuir probes: Floating potential and ion saturation current J. Vac. Sci. Technol. Vac. Surf. Films 24 1366–72
- [7] Ellis H W, Pai R Y, McDaniel E W, Mason E A and Viehland L A 1976 Transport properties of gaseous ions over a wide energy range *At. Data Nucl. Data Tables* 17 177–210
- [8] Tichý M, Šícha M, David P and David T 1994 A Collisional Model of the Positive Ion Collection by a Cylindrical Langmuir Probe *Contrib. Plasma Phys.* **34** 59–68
- [9] Bogaerts A 2009 Hybrid Monte Carlo Fluid model for studying the effects of nitrogen addition to argon glow discharges *Spectrochim. Acta Part B At. Spectrosc.* **64** 126–40